A

An RF Power Source Upgrade to the NLC Based on the Relativistic-Klystron Two-Beam-Accelerator Concept

Contents

A.1 Introduction

There are a number of possible routes to upgrade the center-of-mass energy to 1.5 TeV. The most straightforward is to use the same accelerating gradient as the 1-TeV design, 85 MV/m, and increase the length of the X-band linear accelerators by 50%. This would require extending the 10-GeV trombone arm to incorporate the extra length. In addition, magnets in the final focus and collimation regions would have to be rearranged, but the lengths of these regions have already been sized for the 1.5-TeV upgrade.

Unfortunately, the present power sources which would be used to attain the 1-TeV-c.m. energy, *i.e.*, the 50-MW or 75-MW klystrons and SLED-II pulse compression system, are too inefficient for the 1.5-TeV design; they would require an AC power in excess of 350 MW. There are a number of possible future power sources that might be utilized for the 1.5-TeV NLC such as the sheet beam and cluster klystrons, the Binary Pulse Compression system, and the Two-Beam Accelerator. In this appendix, a more detailed description of a Two-Beam Accelerator source, which has been designed at LBNL and LLNL, is described.

As an rf power source candidate for linear colliders, two-beam accelerators (TBA) [Sessler 1982, Sessler 1987] have the inherent advantage of very high efficiency for power conversion from drive beam to rf. In addition, induction-linac-based TBAs have favorable scalings with high frequencies ($\geq$11.4 GHz) and high accelerating gradients ($\geq$100 MV/m). Conversion of high-current electron beam power to rf power has been demonstrated at the gigawatt level at 34 GHz in free-electron laser experiments [Orzechowski 1986], and at several hundred megawatt levels at 11.4 GHz in relativistic klystron experiments [Allen 1989]. Reacceleration experiments [Westenskow 1994] have successfully demonstrated bunched beam transport through two reacceleration induction cells and three traveling-wave extraction cavities for a total rf output of over 200 MW. The phase and amplitude were shown to be stable over a significant portion of the beam pulse.

The technical challenges for making TBAs into realizable power sources lie in the dynamics of the drive-beam which must propagate over long distances. In particular, the beam breakup (BBU) instability through a long, multicavity, relativistic klystron (RK-TBA) is known to be severe. While BBU suppression techniques have been successfully demonstrated for a few cavities [Haimson 1992, Houck 1992a], a scenario with acceptable BBU control over many traveling-wave cavities must be constructed. Similarly, the longitudinal stability of the rf bunches over a multicavity TBA must be demonstrated. For rf phase and amplitude stability, the induction machine must produce and maintain a beam with constant current and energy over the duration of the pulse. In addition to technical feasibility, a case for economic attractiveness is no less essential for the viability of the TBA. Cost and overall system efficiency are essential elements of an acceptable linear-collider power source.

With these general considerations in mind, a systems study, including physics and engineering designs, as well as bottom-up costing, was conducted for a point design using the RK-TBA concept as a power source for the upgraded Next Linear Collider (NLC) [Siemann 1993]. We refer to this design as the TBNLC. In the following we present the results of the TBNLC system study and our current estimate of total system efficiency of 50%. We also describe an experimental program to reduce the risk of implementing the RK-TBA concept to a large collider. Demonstrations of the key concepts of the TBNLC design are expected to be completed by 2002 at which time the TBNLC could be seriously considered for a 1.5-TeV NLC upgrade. A schematic of a portion of the low-energy e^- side of the TBNLC is shown in Figure A-1.

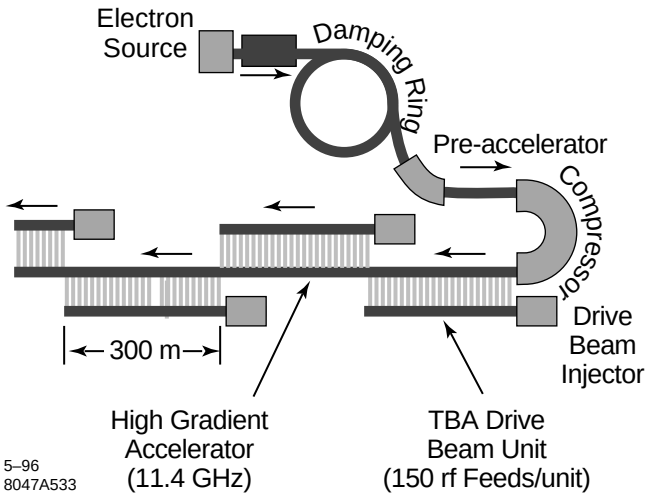

Figure A-1. *Low-energy portion of the e^- side of a linear e^+e^- collider using an RK-TBA design for the rf power source. Our design requires 76 TBA units to provide 1.5 TeV of energy gain.*

A.2 A Design for an RK-TBA-Based rf Power Source

A.2.1 Power Source Requirements

The objective of the TBNLC system study was to construct a conceptual design of the power source for the NLC. Our philosophy was to stay within the design constraints of the NLC and to have a power source system that matches the high-gradient structures being considered for the NLC. However, since the parameters of the NLC were not finalized at the time of the study, we made some choices for power source requirements so that the design and costing studies could be concrete. The design goals for the study were as follows:

Rf frequency	11.424 GHz
Repetition rate	120 Hz
Peak power/structure	360 MW
Distance between extraction structures	2 m
Pulse length (flattop)	200 ns
Pulse rise time	125 ns
Center-of-mass energy	1 TeV

The peak power of 360 MW at 11.424 GHz corresponds to an unloaded gradient of 100 MV/m in the NLCTA high-gradient structures presently tested at SLAC. This power is generated from an extraction cavity in the RK every 2 m, to match the 1.8-m accelerator sections, and to provide adequate spacing in between the HGSs for input and output couplers, focusing, etc.. In the study, we costed the power source for a total of 15 km of this high-gradient structure, 7.5 km for each arm of the collider. There is a total of 7500 rf extraction cavities, with a total peak power of 2.7 TW. The unloaded energy gain from each arm of the collider is 675 GeV. Assuming a loaded gradient that is 75% of the unloaded, final energies of the electron and positron bunches are 506 GeV each.

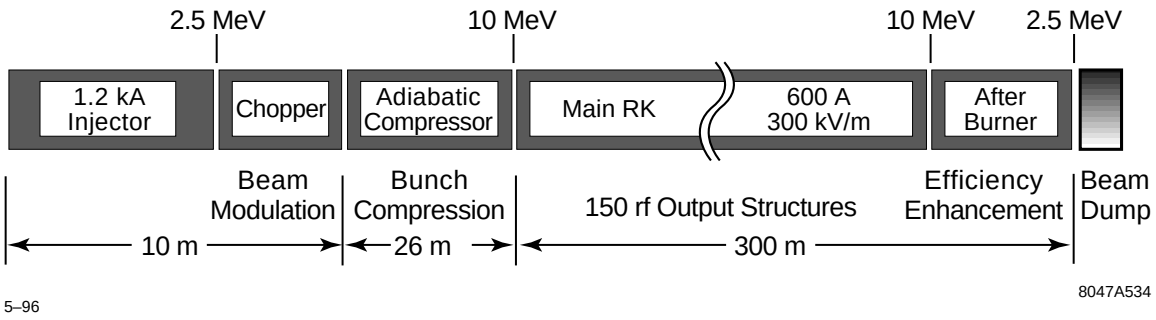

Figure A-2. *Schematic showing major components of the RK-TBA unit.*

The pulse length was determined by the fill time of the structure plus the length of the multi-bunch particle train. To maintain constant particle energy from bunch-to-bunch, the required electric field should grow linearly in the first 100 ns, and remain constant over the remainder of the beam-on time. The flattop is specified as 200 ns, approximately twice the flattop pulse length of the present parameter list (∼100 ns flattop), which allows us to accelerate pulse trains of 143 bunches and leads to a corresponding increase in luminosity. This is possible for our TBA design at only modest cost increase, and is a natural extension of the NLC parameter set to take advantage of the RK-TBA structure. Because of the intrinsically high-efficiency of the RK-TBA, the average power required stays at about 200 MW.

The required electric field at the front of the 100-ns rise is roughly 25% of the asymptotic value. Hence, we specify our input pulse to rise linearly (in field) from zero to its full value in 125 ns. The power increases quadratically over the rise time. This pulse shape can be generated in an RK by a corresponding linear rise in the current waveform of the drive beam, and a linear rise in the reacceleration voltage as well. Further refinement of the pulse shape to match dispersion in the high-gradient structure and to improve energy flatness can be achieved by appropriate shaping of the drive beam current and voltage, but were not considered in the TBNLC study.

A.2.2 TBNLC Architecture

To provide rf power for a 1.5-TeV high-gradient linear accelerator, the TBNLC design requires 76 independent RK-TBA units. Each RK-TBA unit is about 300-m long, and has 150 extraction cavities (Figure A-2). To replenish the 360 MW generated from the extraction cavity every 2 m, the 10-MeV drive beam with average current of 600 A is reaccelerated at 300 kV/m. The design current could be raised slightly to compensate for rf losses in the induction cells (*e.g.,* 625 A for 4% loss). The main body of the RK consists of identical 2-m modules each of which has six 100 kV induction cells and one extraction cavity. Both the drive beam current and reacceleration voltage have a rise time of 125 ns and a 200-ns flattop, with a falltime that is comparable to the rise time.

The front end of each RK consists of an injector in which a 1.5-kA beam of electrons is generated and accelerated to 2.5 MeV. A 5.7-GHz chopper is placed at this point to generate a bunched beam at 11.4 GHz. See Section A.5.3 and Figure A-20 for additional information on the modulation of the beam. Chopping reduces the DC current from 1.5 kA to 600 A. This bunched beam at 2.5 MeV is then accelerated to 10 MeV in an adiabatic compressor section. Bunching cavities in this section further reduce the length of the bunches, and prepare the beam with the right phase space for injection into the main RK. At the end of the RK, there is an afterburner section in which rf extraction continues, but reacceleration is absent. The afterburner allows us to further extract rf power from the bunched beam, and thus enhances the overall efficiency of the RK. At the end of the afterburner, the spent beam (at 2 to 3 MeV) is collected

at a beam dump. The adiabatic compressor section is 26-m long, while the main RK has 138 extraction cavities over 276 m. The afterburner consists of 12 rf cavities, making a total of 150 extraction cavities.

The overall length of a RK-TBA unit is determined by a balance of two opposing considerations. The longer the RK-TBA unit, the higher the overall efficiency, as the overhead losses from the front and the back ends become a smaller fraction of the total power. On the other hand, the control of beam instabilities and beam degradation effects become increasingly more difficult as the overall length is increased. Longitudinal and transverse beam dynamics simulations indicate that the stability of the bunched beam can be maintained in the proposed RK-TBA unit.

The efficiency for conversion of power in the drive beam to rf power is easily evaluated for the proposed RK system. Allowing for some rf loss in the induction cavities, the overall efficiency is estimated to be 90%. The 10% loss is shared among the beam loss on the chopper (3.7%), beam dump (2.8%), and rf into induction cavities (3.6%). The efficiency for wall plug to drive beam is 55%. Hence the total efficiency from wall plug to rf is 50%.

The rf power requirement of 360 MW/2 m determines the product of the accelerating gradient and beam current in the drive beam. Our particular choice of 300 kV/m and 600 A is again based on a balance of two considerations. With higher current and lower gradient, the volume of magnetic material required is reduced and the efficiency is increased. However, beam transport becomes more difficult with increasing current.

The linear rise in the drive beam current assures that the extracted rf field has the right waveform for beam loading in the HGS, while the linear rise in the voltage of the reacceleration cells assures that the entire drive beam stays at 10 MeV from head-to-tail. This is important for both beam transport and for rf phase stability. Hence, the rising portion of the current and voltage generate useful rf power, but the fall portion is wasted. The corresponding loss in efficiency due to finite falltime is included when we consider the efficiency of the pulse power system.

A.2.3 Main RK

The main RK consists of identical 2-m modules. The key elements of a module are the permanent quadrupole magnets for focusing of the drive beam, the induction cells for reacceleration, and one rf extraction cavity. Design considerations for each of these major components is discussed below. The key issues in the design are related to the physics of rf extraction, reacceleration, and transport. However, attention was paid to making the module compact and efficient. The resulting unit has a diameter of 35 cm, which is quite small compared to existing induction accelerators. A schematic of the 2-m module is shown in Figure A-3.

Pipe size

In the design of induction accelerators, the size of the beam tube is usually determined by BBU considerations, since the transverse impedance from the acceleration gap is inversely proportional to the square of the pipe radius. In our RK design, the low-frequency BBU arising from the induction gaps is ameliorated by the low-beam current of 600 A and Landau damping associated with the energy spread inherent in the rf buckets. With proper attention to the gap geometry, we were able to design a pipe with a radius of 2.5 cm, and predict acceptable BBU growth.

Permanent magnet focusing

The small pipe radius allows us to take full advantage of permanent magnets, which have significant cost advantages when the focusing systems are small. Another major reason for using permanent magnets is the associated efficiency, as they eliminate the need for power supplies.

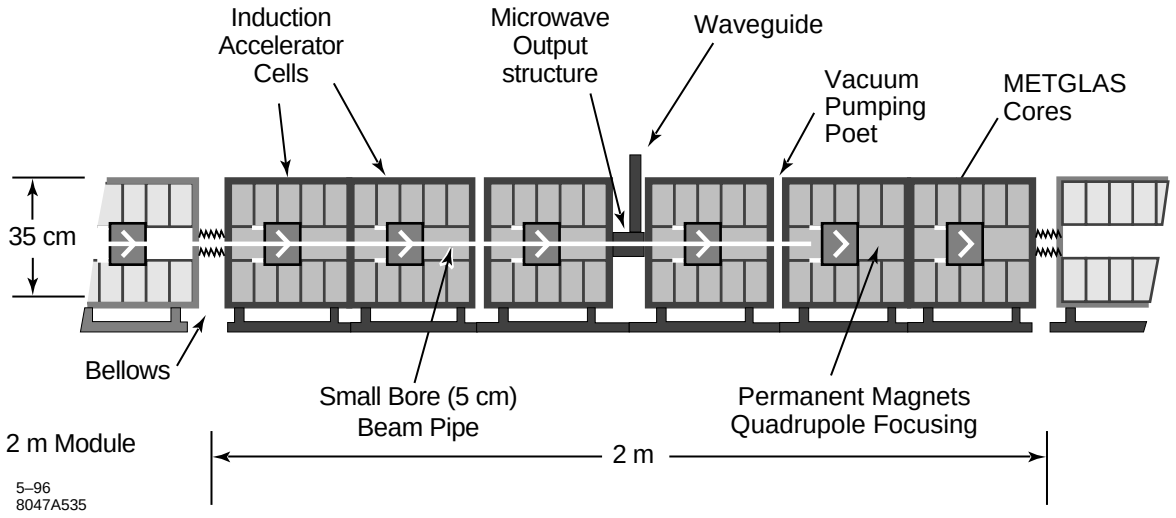

Figure A-3. *Schematic of 2-m RK Module*

Several basic considerations govern the design of the FODO lattice. The foremost requirement is associated with a technique concocted to minimize the high-frequency BBU growth arising from the HEM_{11} mode in the rf extraction cavities. To suppress the instability growth, we demand that the betatron period be equal to the distance between adjacent extraction cavities,*i.e.,* 2 m. In addition, the phase advance per lattice period must be less than 90° to ensure beam stability. Finally, the focusing strength must be sufficient to keep the beam envelope small enough to stay within the beam tube.

The zeroth-order design equation is given by the thin lens approximation

$$\sigma_0 = \frac{\eta B L^2}{R[B\rho]} \tag{A.1}$$

where σ^0 is the phase advance per lattice period, and B is the quadrupole field strength at pole-tip with radial position R. L is the half-lattice period, and η the occupancy factor for the quadrupole. The rigidity of the electron beam is given by

$$[B\rho] = \frac{\beta\gamma mc}{e} \tag{A.2}$$

where $\beta\gamma mc$ is the momentum of the relativistic beam, and $[B\rho]$ has the value of 0.035 T-m for 10-MeV electrons.

A first-order correction for deviations from the thin-lens approximation is obtained by replacing the phase advance and occupancy factor with scaled variables given by [Barnard 1991]

$$\hat{\sigma}_0 = \sqrt{2(1-\cos\sigma_0)} \quad \text{and} \quad \hat{\eta} = \eta\sqrt{2\left(1-\frac{2\eta}{3}\right)} \tag{A.3}$$

In our design, we use σ_0 of 60°. There are 12 half-lattice periods in 2 m. The physical occupancy factor is 0.48. The modified thin lens formula then gives a B-field at pole tip of 800 Gauss. This estimate is within a few % of the actual B-field required to give a 2-m betatron period, when we include realistic spatial profile of the magnetic field, as well as the energy variations of the drive beam as it is accelerated over the 2-m module.

A preliminary quadrupole design was constructed by Klaus Halbach [Halbach priv, Halbach 1980]. It consists of four rectangular blocks of ferrites with residual field B_r of 3.2 kg. The dimensions of the blocks are 1.1 cm $\times$ 3.22 cm $\times$ 8 cm. This design has as the first nonzero harmonic $n = 10$, with 8.6% strength of the quadrupole field at aperture radius. Finite differential permeability effects have not been included in this preliminary design.

A basic requirement of the transport channel is that the focusing strength must be sufficiently strong to keep the beam from hitting the beam tube. The beam envelope in the focusing channel can be estimated from the equilibrium formula

$$\frac{\varepsilon^2}{a^2} = \sigma_0^2 \left(\frac{a}{L}\right)^2 \tag{A.4}$$

where $\varepsilon = \varepsilon_n/\beta\gamma$ and a are respectively the unnormalized edge emittance and the edge radius of the beam envelope. With a normalized edge emittance of 600 mm-mr, (which is achievable with a good gun design), we obtain an edge radius of about 2 mm for the beam.

Steering and Focusing Corrections

Steering and focusing corrections are achieved in the design by means of low-field ($\sim$10 Gauss) DC coils located in the region immediately outside of the permanent magnets, at radial positions of about 4 cm from axis. These correction coils can be manufactured inexpensively on printed circuit boards.

Since the beam apertures are small, particularly around the extraction cavities, beam centroid displacements must be kept to a minimum. Quadrupole misalignments, when combined with energy variations from head to tail, can lead to beam offsets that change over the length of the pulse, *i.e.*, the corkscrew phenomenon [Chen 1990]. Our strategy for minimizing beam displacements and associated corkscrew is to impose misalignment tolerances that are not excessively tight, design for energy flatness of $\leq$1%, and to correct alignment errors with closely spaced dipole-steering coils. Detailed steering algorithms have not been worked out yet, but for the purpose of costing, we provide three sets of steering coils and two beam position monitors per betatron period.

A key ingredient for the suppression of high-frequency BBU is that the betatron period be equal to the distance between adjacent cavities. To ensure that this requirement is obeyed, a feedback system with two correction quadrupoles per betatron period is incorporated into the design. A possible monitor for the betatron motion is to use the rf output from the extraction cavities at the dipole frequency. Whether the signal sensitivity is adequate for this purpose needs further study.

Induction Cores

The design of induction cells for reacceleration is based on the relation

$$V \cdot (\Delta t) = A \cdot F_p \cdot (\Delta B) \quad , \tag{A.5}$$

where the core size (with magnetic flux over area A and F_p is the packing factor, or the fraction of the total core that is occupied by magnetic material) is determined by the required voltage V and pulse length Δt. The allowed flux swing ΔB is different for different magnetic material. Our design uses METGLAS®[1] with ΔB of $\sim$1.3 T. Flux swings for METGLAS are several times larger than ferrites, for example, which are commonly used in short-pulse induction machines such as the Advanced Test Accelerator (ATA) [Kapetanakos 1985] and the Experimental Test Accelerator II (ETA II) [Clark 1988]. The cores are correspondingly more compact. Furthermore, METGLAS is quite inexpensive, particularly when bought in large quantities.

[1] METGLAS® is a registered trade name of Allied-Signal.

To determine the transverse dimensions of the core, (with outer radius R_o, and inner radius R_i), we recast Eq. A.5 in terms of the accelerating gradient G and core occupancy factor η_c (fraction of the axial length occupied by induction cores) as follows:

$$R_o - R_i = G\Delta t/(\Delta B \eta_c F_p) \tag{A.6}$$

where F_p has a value of 0.65 to 0.75 for typical METGLAS cores. Since the accelerating gradient and pulse length are fixed by overall system requirements, our design philosophy was to maximize axial core occupancy. The proposed design has η_c of 0.75 and core thickness $R_o - R_i$ of 10 cm.

Compact cores reduce cost as well as energy loss. Empirical measurements of core losses can be parameterized to give the following phenomenological formula for the core current (in Amps):

$$I_c = 360(R_o + R_i) \cdot (\Delta B/\Delta t) \tag{A.7}$$

where the radial dimensions are in meters, ΔB in tesla, and Δt in microseconds. The fraction of energy lost in the core ($I_c/I_{\rm total}$) is proportional to the size of the core. Our design parameters give a core current of about 117 A. With a 600-A beam, the core efficiency is 80%. See Section A.4.2, "Induction Accelerator Module", for results of core testing.

The magnetic material in a 2-m module is packaged into six independent 100-kV induction cells. Each cell in turn consists of five 20-kV cores. Packaging into small induction cores provides a natural match to the low-voltage pulse power system. Figure A-4 is an illustration of the proposed induction cell showing the five cores.

Pulsed Power

The desired voltage pulse from each core has a 125-ns linear rise, followed by a 200-ns flattop at 20 kV, followed by a fast fall. This voltage waveform is generated with pulse forming networks (PFNs) with tapered impedance to match the induction core. Power input to the PFNs consists of a DC power supply and a Command Resonant Charging unit. The entire pulse power train is at low voltage, and no step-up transformers are needed. Hence, high efficiency and low cost is possible.

Acceleration Gap

Each 100-kV induction cell has an induction gap, which is one of the more critical components of the design. Ongoing design efforts evolve around the following key issues:

- **Reduction of high voltage breakdown risks.** To have an induction gap that is safe from breakdown, the gradient across the insulator must be sufficiently low (<30 kV/cm), sufficiently low fields on the metal surfaces (<100 kV/cm), proper shielding of the insulators from secondary electrons and X-rays generated by the beam, and proper design of the triple-point (the interface between insulator, metal, and vacuum).
- **Suppression of low-frequency BBU.** Dipole modes associated with the gap (at a few GHz) can lead to severe problems if not carefully damped. The required transverse impedance was achieved with heavy de$Q$ing by placing microwave-absorbing material at critical locations around the gap.
- **Reduction of transverse and longitudinal impedances at high frequencies.** While the high-frequency BBU (HEM_{11} mode at ~14 GHz) is generated primarily in the rf extraction cavities, and the major BBU suppression activities center around them, one must be careful to ensure that the transverse impedance contribution from the induction cavities are indeed negligible. In the present designs, the transverse impedance around 14 GHz can be

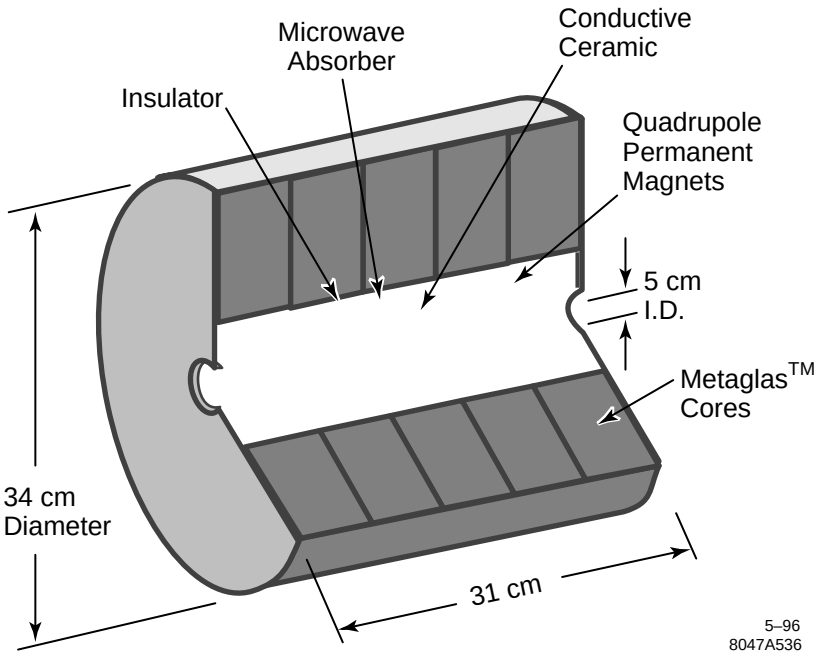

Figure A-4. *Proposed RK induction cell design.*

made to be lower than half an ohm, and its effect on the high frequency BBU is insignificant. The longitudinal impedance at 11.424 GHz must be low to minimize the microwave power loss. Our design goal is to maintain the induction gap loss to less than 4%, which requires that the longitudinal impedance be less than 2.4 Ω. Present designs are approaching the required impedance.

RF Extraction Cavities

Design of the rf extraction cavity is a major ongoing activity in theory and simulations. Present designs evolve around traveling-wave structures with three cells of eight-mm inner radius. The rf output is extracted through two separate ports in the third cell, with 180 MW each transported through separate waveguides, and fed directly into the two input couplers of the high-gradient structure. An illustration of a proposed design is shown in Figure A-5. Detailed design of the cavities centers around five key issues:

- **Required output power.** The extraction cavity must have the right effective impedance of about 540 Ω to extract 360 MW from a highly bunched beam (70° microbunch length) whose first harmonic current at 11.424 GHz is about 1.15 kA.
- **Minimal breakdown risks.** Our present designs use traveling-wave structures with three cells to reduce the surface fields. Surface-field gradients of less than 70 MV/m appear possible.
- **Inductive detuning.** In addition to generating the right amount of power, the rf cavities provide continuous longitudinal bunching for the drive beam. This is accomplished by inductively-detuned traveling-wave-structures.
- **Dipole de$Q$ing.** The rf cavities must have low-transverse impedances for the suppression of BBU. Fortunately, there is a natural de$Q$ing mechanism, as the required extraction cavities have inner radii of around 8 mm, and the

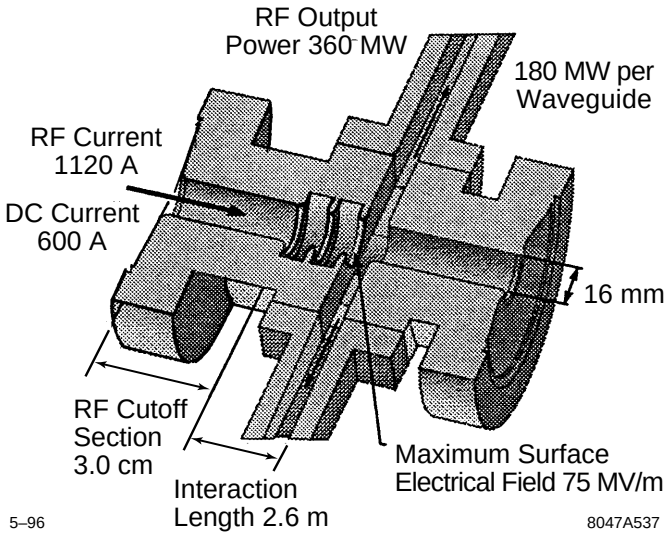

Figure A-5. *Illustration of an rf extraction structure.*

dipole modes in the cavity couple to the TE_{11} mode in the pipe. Simulations to date suggest that the resulting impedances are sufficiently low for BBU suppression provided that the Betatron Node Scheme is used.

- **Transverse focusing.** The rf cavities have transverse fields associated with the fundamental mode. They can degrade the beam envelope if they are sufficiently strong and/or not properly corrected. Evaluation of these transverse forces from theory and simulations is ongoing.

A.2.4 Front End and Back End

Each RK unit has a front end that consists of an injector, a chopper, and an adiabatic compressor section. At the end of each RK unit, there is an afterburner, followed by a final beam-dump. These five elements are described below.

Pre-chopper

The injector is basically a short-induction accelerator to generate an unbunched 300-ns electron beam at 2.5 MeV. This section may consist of an induction injector (at 1–1.5 MeV), followed by a short-induction accelerator section that takes the beam to 2.5 MeV. The required current from the injector is 1–1.5 kA, depending on the efficiency of the chopper which is required to produce at its exit a bunched beam with a DC current of 600 A.

The current waveform required consists of a linear rise over 100 ns, followed by 200 ns of flattop. The beam energy should be constant over the entire 300 ns, including the front portion with the rising current. To generate the linearly rising current, the voltage pulse in the 1-MeV injector will also, by the Child-Langmuir Law, have a (nonlinear) 100-ns rise time. The PFN in the subsequent short accelerator section must be arranged to produce a higher voltage at the beam front, thereby compensating for the low-energy at the injector exit.

Since the electron beam will be transported over 300 m of narrow pipes, caution must be taken to minimize head-to-tail energy variations, as well as transverse beam offsets and beam temperature. The injector design should produce a

bright beam with a normalized edge emittance of 600 mm-mr or less, and transverse displacement of 200 microns or less.

Chopper

The purpose of the chopper is to generate cleanly-separated microbunches at 11.4 GHz. The basic scheme follows the design of Haimson Research Corporation's Choppertron [Haimson 1989], a 11.4-GHz microwave generator that has been deployed at LLNL. A subharmonic dipole deflecting cavity at 5.7 GHz causes the electron beam to oscillate about a limiting aperture, leading to chopped bunches at twice the oscillating frequency. A similar device can serve as the TBNLC front-end chopper, except that much more effective heat dissipation is required for the 120-Hz operation of the NLC upgrade.

Since a substantial amount of energy is lost on the chopper, there is incentive to make it more efficient. One idea is to precede the subharmonic deflecting cavity with conventional bunching cavities at 11.4 GHz. The role of the chopper then is primarily to clean up the particles with the wrong phase. This requires straightforward phasing of the 5.7-GHz input power to the deflecting cavity relative to the incoming prebunched beam.

Adiabatic Compressor

The exiting beam from the chopper has microbunch lengths equivalent to 180° or greater in longitudinal phase space. In the adiabatic compressor region, the microbunch lengths are further reduced to 70°, which is the needed bunch length for long-distance propagation in the main RK. This is accomplished by a number of idler cavities that are more inductive than the rf extraction cavities in the main RK.

In addition to microbunch sharpening, this section also serves to provide the energy transition from 2.5 MeV to 10 MeV. The induction core structures are very similar to the main RK. However, the voltage waveform should be flat over the 300 ns of beam-on time, so that the head-to-tail energy flatness required for phase stability could be maintained at 10 MeV.

The quadrupole magnets are weaker at the lower energies, and continues to increase with increasing energy, so that the betatron wavelength is kept fixed at 2 m. Structurally, the adiabatic compressor section looks very similar to the main RK, except that no power is extracted from the idler rf cavities.

Afterburner

At the end of the RK is an afterburner section, the primary purpose of which is to increase overall system efficiency by extracting more power out of the bunched beam at the end of the main RK. This section has a number of rf extraction cavities, permanent magnets for focusing, but no reacceleration cells. The spacing of the rf cavities is changed as the average energy of the beam continues to decrease. The impedance of the cavities is also modified to compensate for changes in the rf bucket. The TBNLC design has 12 cavities in the afterburner section, each generating 360 MW, and together covering a total of 12 m.

Beam dump

As the spent electron beam reaches the final beam dump, its average energy is less than 3 MeV. The design of this component is straightforward.

A.2.5 The Key Ideas

A few key ideas underlie the whole design of the relativistic klystron for the TBNLC and are summarized as follows:

- **Betatron Node Scheme for high frequency BBU control.** The most severe BBU instability is associated with the HEM_{11} transverse mode in the rf extraction cavities. Strong suppression of this mode is achieved by introducing a Betatron Node Scheme [Li 1994] in which adjacent rf extraction cavities are placed exactly one betatron period apart. This scheme minimizes beam centroid displacement which excites the transverse mode, and alters the nature of the instability from exponential to a slow secular growth.
- **Landau damping for low-frequency BBU suppression.** Quite apart from the high-frequency dipole mode associated with the rf cavities, there is a low-frequency (a few GHz) dipole mode associated with the induction reacceleration gaps. This BBU instability is ameliorated by Landau damping due to a large energy spread inherent in the rf buckets of the bunched drive beam. Combining this feature with dipole mode suppression measures in the induction gap design, the calculated low-frequency BBU growth is minimal.
- **Inductively detuned cavities for longitudinal beam stability.** To maintain tight rf bunches over long distances with multiple extraction cavities, the rf output structures are inductively detuned. While the concept of inductive detuning is not new, the theoretical framework has to be developed and implemented in simulation codes for traveling wave output structures. Cavity parameters required for stable beam propagation through multiple structures were determined in the TBNLC system study.
- **Small low-cost induction cells.** The induction cells in the TBNLC design are about one foot in diameter, much smaller than most of the existing induction machines. This design was possible because of three key features:
  - Use of METGLAS for the induction cores. This is a low-cost magnetic material that can accommodate a large flux swing.
  - Use of low-field permanent magnet quadrupoles. The relatively high drive beam energy of 10 MeV (compared to klystron beams) is a natural match to a strong focusing transport system with low-cost ferrites. An additional advantage of permanent magnets is, of course, the elimination of power supplies.
  - Narrow beam pipes—the design pipe diameter of 5 cm is much smaller than other existing high current machines. This is possible because of the relatively low current (by induction machine standards) of 600 A, and the low-frequency BBU suppression features described earlier. Large beam pipes in usual induction machines are dictated by BBU considerations.
- **Low-voltage pulse power system for efficiency and cost.** The induction cell design matches naturally to a 20-kV system with PFNs triggered by ceramic thyratrons and powered by DC power supplies and command resonant charging systems. This system does not require step-up transformers and eliminates losses associated with a high-voltage system.

A.3 TBNLC Physics Studies

The TBNLC system study addressed the issues of longitudinal and transverse stability of the drive beam and the related areas of rf extraction cavity and induction cavity designs.

A.3.1 Longitudinal Beam Dynamics

Longitudinal stability of the drive beam is among the important issues for the demonstration of technical feasibility of the RK-TBA concept. In the TBNLC design, the drive beam is required to stay bunched longitudinally over 150 extraction cavities. Space charge effects cause initially tight bunches to expand. The debunching process is further aggravated by the energy spreads along the bunches as they interact with rf fields. In usual traveling wave extraction cavities, rf waves are in synchronism with the drive beam and debunching becomes very severe after a few cavities. Beam debunching, if uncompensated, will result in reduced power extraction in subsequent cavities. To overcome this problem, we employ a scheme in which the drive beam is not synchronous with the operating wave mode; more specifically, the phase velocity of the rf field is larger than the speed of light so that the bunches always lag behind the wave. This is what we call inductive detuning and can effectively bunch the beam. The concept of inductive detuning is well known for standing wave structures (SWSs), *e.g.,* the penultimate cavity in a klystron, in which the frequency of the cavity is detuned from the resonant frequency. For the traveling wave structures (TWSs) of our RK, the approach we take is to keep the frequency ω of the operating mode unchanged, but reduce its wave number k, such that the wave field advances faster than the beam. In this case particles at the front of the bunch lose more energy and slow, while particles at the tail of the bunch lose less energy and catch up. This mechanism causes a continuous sharpening of the bunch, thus counteracting the debunching forces. The resulting longitudinal phase space continues to rotate in a stable rf bucket with a relatively stable bunch length. Thus both constant power extraction and beam bunching can be achieved simultaneously.

Parameters for the detuned rf output structures were estimated from analytical expressions developed during the TBNLC system study. Numerical simulations were then performed using the relativistic klystron code RKS [Ryne 1990]. This code solves self-consistently the single-particle equations of motion for the beam and the coupled circuit equations that govern the cavity excitation, and it includes the calculation of the space charge effect. It assumes a single-dominant mode and cylindrical symmetry of its fields inside the cavity.

Figure A-6 presents the output power from each of 150 TWSs in the main RK section for both a successful inductive detuning case and its corresponding synchronism case. The parameters for the inductive detuning case are given in Table A-1. For the synchronism case, the level of the extracted power $P_{\rm out}$ declines sharply due to the space charge debunching effect as the drive beam traverses the RK. In contrast, when the TWSs are properly detuned, the rf bucket can remain stable and output power can be sustained at the desired level ($\sim$360 MW) for the 150 extraction cavities.

The synchronism case in Figure A-6 consists of conventional three-cell TWSs operating at the $2\pi/3$ mode. In the inductively detuned case the operating detuning angle is 30°. The cavity is therefore operating in a $\pi/2$ mode (*i.e.,* phase advance of the field across one cell is 90°). The longitudinal dimension of each cell is the same in the two cases while the transverse dimensions are varied. URMEL and MAFIA codes were used for detailed cavity design.

A key feature for RK design is the cavity filling time, *i.e.,* the time it takes for the rf field in a cavity to reach equilibrium state. In Figure A-7, we present the time dependencies of output power at the 50th, 100th and 150th extraction cavities for the inductive detuning case in Figure A-6. It shows that after about 15 ns, the fields in all the cavities reach their equilibrium states. This indicates that the erosion on the beam head due to the cavity filling process is not serious. The short fill time is a result of low Q and high V_g.

Further RKS code simulation studies were conducted to examine the sensitivity of the inductive detuning scheme to the important parameters of bunch length and detuning angle. For 30° of detuning, the scheme was insensitive to variation in bunch lengths from 50° to 90°, although performance deteriorated for lengths above 90°. Similarly, the scheme was insensitive to increasing the detuning angle from 30° to 35°, but performance deteriorated for angles below 30°.

The issue of radial defocusing, or emittance growth, due to the interaction of the beam with the rf fields in the extraction structures is an active area of study. The underlying theory of the RKS code involves power balance. Detailed rf

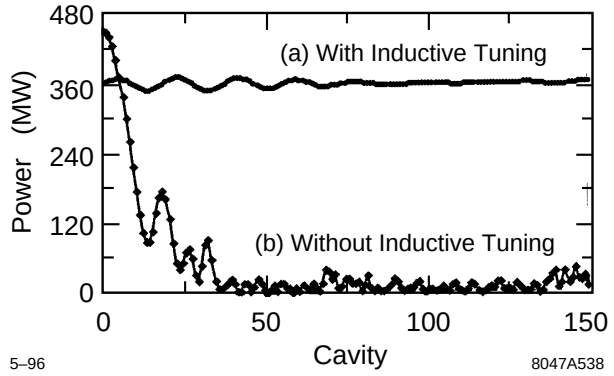

Figure A-6. *Power extraction from 150 cavities in one unit of RK-TBA: (a) With inductive detuning ($\Delta = 30^{\circ}$, phase velocity 1.33 c); (b) No inductive detuning ($\Delta = 0^{\circ}$, phase velocity 1.0 c).*

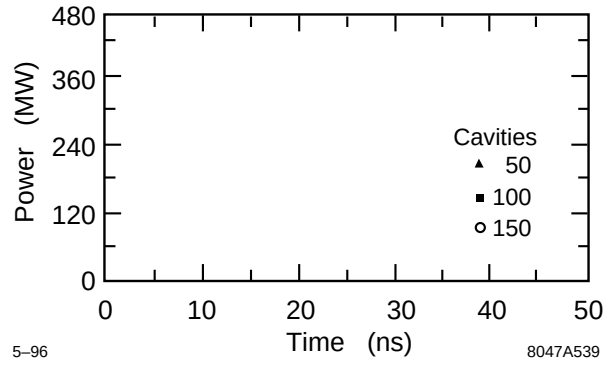

Figure A-7. *Time evolutions of output power at 50th, 100th and 150th TWSs for the nonsynchronism case in Figure A-6.*

field information is less stringently modeled. This approach works satisfactorily for standing wave and synchronous traveling wave structures. However, for detuned traveling wave structures, the RKS code does not adequately account for radial forces on the beam limiting its usefulness for extended structures to 1-D simulations.

A.3.2 Transverse Beam Dynamics

The excitation of transverse beam instabilities due to higher order modes has been identified as a major issue in the design of a long multicavity RK-TBA. The narrow aperture and high average current of the RK accentuates the problem. There are two separate structural components that contribute to the transverse instability. The induction module with an aperture of 5.0 cm has a trapped dipole mode around 3 GHz and the output structure with a 1.6-cm aperture has a transverse mode near 14 GHz. Both modes can interact strongly with the beam. The effect of these structures on transverse instability can be studied separately due to the difference in resonant frequencies.

Drive frequency	11.424 GHz
Forward traveling mode	TM_{01}
Number of cavities	3
Phase shift per cavity	90°
Wave length	2.626 cm
Phase velocity	1.33 c
Group velocity	0.28 c
Shunt impedance per cell $(R/Q)^*$	27.0 (Ω)
Eigenfrequency for the first 2 cells	11.424 GHz
Eigenfrequency for the 3rd cell	11.666 GHz
Wall-dissipation quality factor	7000
External quality factor for the 3rd cell	6.5
Aperture inner radius	8 mm
Aperture outer radius	12.5 mm
Iris thickness	2.5 mm
Longitudinal dimension of each cell	8.754 mm
Beam energy	10 MeV
Beam current (peak)	600 A
Bunch length	0.51 cm
Beam radius (rms)	2.5 mm

*Traveling-wave shunt reactance is twice the standing-wave shunt reactance.

Table A-1. *Parameters related to the inductive detuning case.*

Low-Frequency BBU

There are three induction modules per meter through the RK. Although considerable damping can be accomplished by the insertion of absorbing material, design constraints imposed by maximum surface electrical fields and vacuum requirements preclude complete damping of higher order modes. Modeling the module's gap as a cylindrical resonator with an impedance boundary condition on the outer wall [Brigg 1985] and assuming an optimum design, the transverse impedance, $Z_{\perp 1}$, will be on the order of 4,000 Ω/m.

Analytical theory [Panofsky 1968] indicates that the transverse instability will grow exponentially along the length of the accelerator. Experience with ATA and ETA II indicate a growth of 4 to 5 e-folds from noise is tolerable in the transverse instability. For a 10-MeV e-beam, using a betatron wavelength of 2 m, a current of 600 A, and gap spacing of m/3, a theoretical estimate of the maximum tolerable transverse impedance of the module, $Z_{\perp 1}$, is about 573 Ω/m. Thus, additional measures are needed to suppress the transverse instability.

The most promising technique for suppressing the transverse instability is Landau damping. To maintain longitudinal equilibrium, inductively detuned rf extraction structures are used. The resulting rf buckets have an intrinsic spread in beam energy over the microbunch on the order of $\pm 7.5\%$. Hose instability theory [Lee 1978, Houck 1993] can be used to estimate a maximum $Z_{\perp 1}$ of about 5,178 Ω/m for total suppression of the low-frequency BBU growth. Theoretically, we can build a suitable induction module to avoid BBU.

The OMICE code [Houck 1992b] was used to model the growth of the transverse instability. In Figure A-8, relative growth in the displacement of the beam's centroid from axis as a function of distance along the axis is shown for several different energy spreads. The finite number of beam slices used in the OMICE code did not permit the level of phase mixing available in a physical beam. Thus, the simulations presented provide a conservative upper bound.

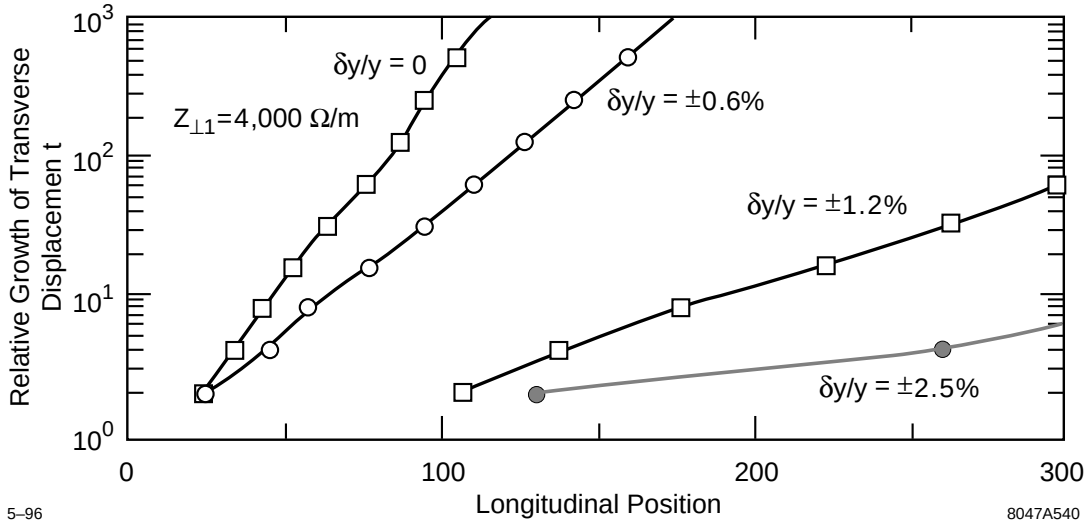

Figure A-8. *Effect of energy spread on the low-frequency instability.*

Table A-2 lists additional input parameters used in the OMICE code. The seed perturbation for exciting the instability was a sinusoidal oscillation of the centroid's transverse displacement at the instability frequency. The conclusion from the numerical modeling is that the instability growth will be acceptable for $Z_{\perp 1}$ less than or equal to 5,400 Ω/m and energy spreads of $\pm 2.5\%$ or greater.

High-Frequency BBU

There is one three-cell, traveling-wave, output structure (TWS) every 2 m through the RK. In the context of the TBNLC design, we limit the growth of the transverse beam displacement to 4 to 5 e-folds over the 300-m system, or 150 TWSs. To keep BBU to this level, we need to minimize and/or suppress excitation of the higher order (transverse) modes in the TWSs.

The contribution of the output structures to the transverse instability of the beam is greater than that of the induction cell gaps for several reasons. The output structure has a smaller aperture to obtain the desired longitudinal shunt impedance. Damping of the higher order modes must not affect the fundamental mode used for power extraction. Also, the three cells comprising the TWS are electromagnetically coupled. Within a TWS, the regenerative BBU mechanism will increase the interaction of the higher order modes with the beam.

The basic design of the output structure has a transverse shunt impedance ($Z_\perp/Q$) of about $3\,\Omega$ per cell. This is significantly lower than for the induction cell gaps. However, the $Q_{\rm wall}$ of the cells is high, on the order of several thousand. The third cell has two output ports that remove energy from the higher order modes. This produces an effective $Q_{\rm ext}$ of about 15. In addition, fields in the first and third cell couple strongly to the TE_{11} mode of the connecting pipe, thus leading to a drastic reduction of Q in both of these cavities. The growth in the transverse instability is also reduced by Landau damping due to the energy spread on the beam. However, even with these instability reduction features, the high-frequency BBU growth is still too high.

The Betatron Node Scheme [Li 1994] was used to limit the growth in the transverse instability to an acceptable level. Figure A-9 shows the large difference in BBU growth as we vary the focusing field from the optimum for the Betatron Node Scheme. This is especially true for the case with a high-Q value for the first cavity. A list of the pertinent

BBU frequency	3.0 GHz
$Z_{\perp 1}$ (Ω/m)	5,400
$Z_{\perp}/Q$ (Ω)	42.972
Cell Q	2
Gap width	2.5 cm
Average beam energy	10 MeV
$\Delta\gamma(\gamma_{\max} - \gamma_{\min})$	3
Current (DC component)	0–600 A in 100 ns
	600 A flattop for 200 ns
Focusing system	Quadrupole - 2-m period
Time step	1/600 ns

Table A-2. *Input parameters for simulated induction cell gaps.*

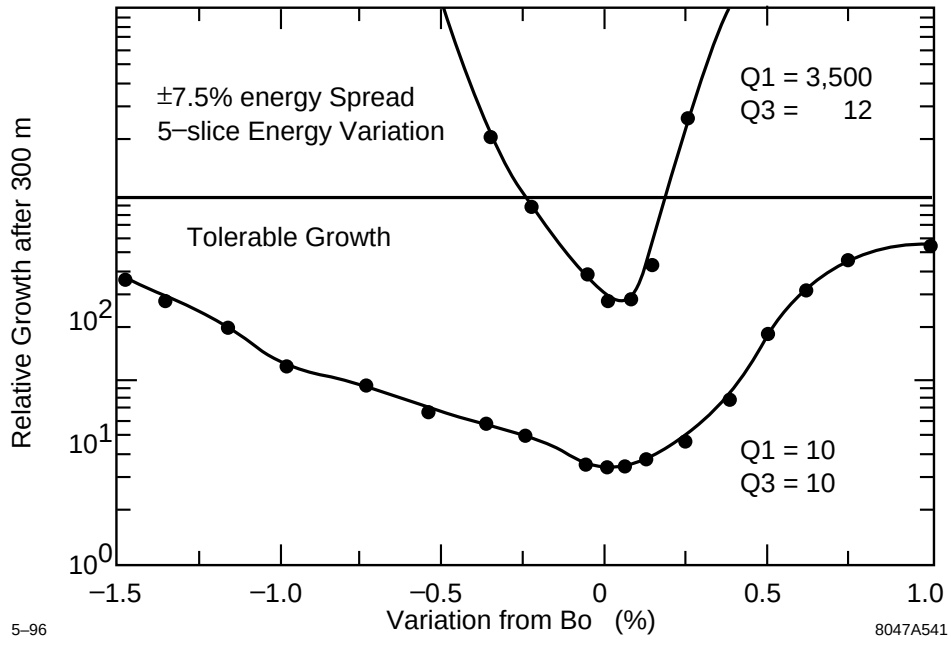

Figure A-9. *Relative growth after 150 TWSs vs. variation from the optimum focusing field. Comparison of an aggressively lowered Q to a high-Q for the first cell.*

Transverse mode	HEM_{11}
Frequency of mode ω_o	14.1 GHz
Number of cells/TWS	3
Electrical length of each cell L_c	8.754 mm
Phase advance/cell ϕ	120°
Group velocity v_g	0.25c
$Q_{\rm wall}$ (1st and 2nd cells)	3,500
Typical $Q_{\rm damped}$	15
$Z_\perp/Q$ for each cell	3 Ω
Current (DC component)	0–600 A in 100 ns 600-A flattop
Pulse length	300 ns
Average beam energy	10 MeV
Quadrupole field	0.0812 T

Table A-3. *Base parameters for simulated traveling wave structures.*

variables, and their base values, is given in Table A-3. The Betatron Node Scheme works well in principle; the key issue is the robustness of the scheme to deviations in the betatron wavelength resulting from errors in focusing field and/or beam energy, as well as sensitivities to cavity parameters.

The main effort of the numerical studies was to delineate the acceptable parameter space. The OMICE code was used to model the time-dependent transverse behavior of a 300-ns pulse over the 300-m length of the RK. An initial constant offset of the beam centroid was used as the seed perturbation for exciting the instability. Base parameters were varied individually to characterize the system's sensitivity to different design parameters such as effective impedance, Q values of the cells, quadrupole focusing field strengths, and variation in average beam energy.

The conclusion of this parameter study was that the Betatron Node Scheme is a promising means for controlling the high-frequency instability caused by these structures. Requirements on energy flatness and field accuracy are quite acceptable ($\pm$1%) provided that the output structures are indeed strongly de$Q$ed. Feedback schemes may further relax the requirements on field and energy accuracy.

A.3.3 RF Extraction Cavity Design

The most basic requirement for the cavity design is that it generate 360 MW of rf power for a drive beam current of 600-A DC and 1–1.5-kA rf current. The cavities must also be inductively detuned to maintain longitudinal beam stability over long distances. The surface fields of the cavity must be sufficiently low to avoid breakdown. Finally, the cavity must have low transverse shunt impedance in order to minimize the high-frequency BBU. The required cavity parameters have been discussed in Sections A.3.1 and A.3.2. In this section, we present electromagnetic calculations to determine the structure of the extraction cavities. We chose in this design effort one specific path to meet the general requirements. The procedure adopted is by no means unique, and we anticipate further optimizations and more detailed calculations in the future.

The numerical tools we have used are URMEL and SUPERFISH for 2-D frequency domain calculations, ABCI and TBCI for 2-D time-domain calculations, and MAFIA for 3-D frequency as well as time-domain calculations. The design procedure is carried out in several steps, starting with the simplest approximations, and adding more realistic features with each successive iteration. The successive approximations are summarized as follows:

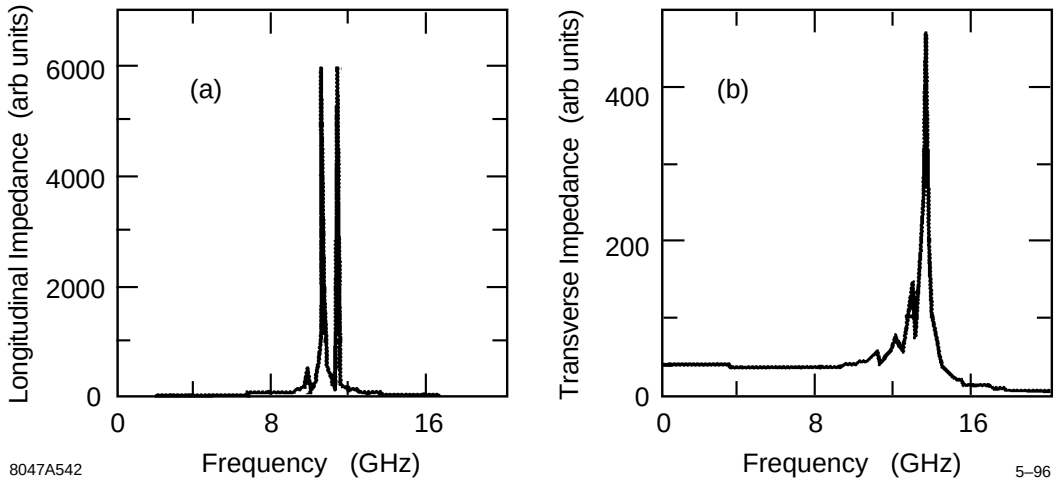

Figure A-10. *Longitudinal and transverse impedances of a three-cell structure with beam pipes.*

- Step 1. We construct a three-cell, disk-loaded, synchronous traveling-wave structure. Desired power extraction determines $(R/Q)/v_g$. URMEL is used to study an infinitely periodic structure, the inner radius a and outer radius b of the structure is varied, and the set of solutions with $v_p = c$ is obtained following the procedure of Thompson *et al.*, [Thompson 1993].
- Step 2. The inductively-detuned structure is constructed by a variation of Step 1. We want the resonant frequency to remain unchanged, but the wavelength increased by a factor of 1.33. The R/Q and v_g for the new configuration are determined with URMEL. The geometry is adjusted to ensure that the R/Q and v_g provide the right power extraction.
- Step 3. Finite beam pipes are then included to model the finite cell structure. The effect of the modified geometry on the field configuration and cavity parameters is then studied.
- Step 4. The 3-D aspects of the output ports are studied using MAFIA. The geometry of the output is varied to achieve the value of Q and ω for proper matching.

The relevant dipole cavity parameters for BBU considerations and the field enhancement factor for assessing the surface field are also determined.

Longitudinal and transverse impedances for the proposed extraction structure are shown in Figure A-10. The field pattern from a MAFIA run is shown in Figure A-11. The pertinent parameters of the structure are given in Table A-3. The determination of the external Q of the 3-D cavity with output structure is based on the Kroll-Yu method [Kroll 1990]. A $Q_{\rm ext} \approx 80$ was calculated for various waveguide iris apertures. The theory in Section A.3.1 was used to estimate the Q of individual cells. Initial estimates suggest that the transverse mode Q for the first and last cavities is as low as 10.

A.3.4 Induction Cavity Design

The interaction of the induction cell gap with the beam is a critical issue for the RK. There are three major criteria that the cell gap must meet: hold-off of the applied 100-kV voltage, low transverse impedance for BBU minimization, and

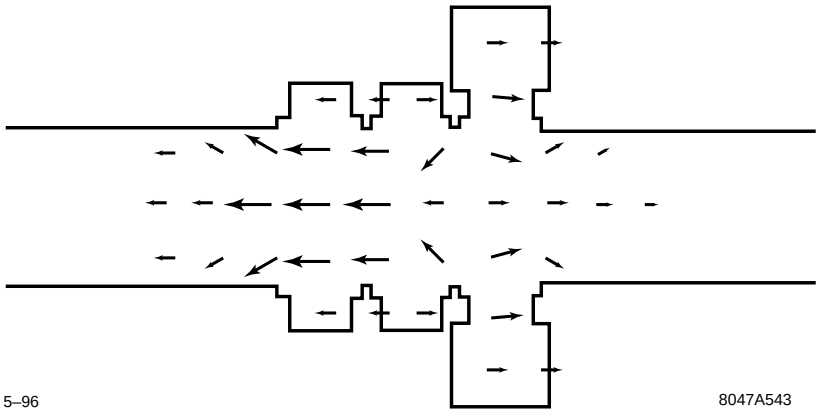

Figure A-11. *Field configuration for the $\pi/2$ mode of the 3-D cavity with output structure.*

Material	ε'	ε''	$\mu\prime$	μ''
Ferrite[a]	13.0	0.0	1.0	9.4
TDK[b]	25	3.3	1.9	2.1
Carbon-loaded ceramic[c]	5.9	1.07	1.0	0.0

[a] Ferrite is modeled after the ferrite used in the ATA induction cells [Deford 1990a], measured at 1 GHz.

[b] TDK Electronics Co., LTD., Absorber IR-B006, measured at 2.5 GHz.

[c] University of Maryland ceramic [Calame 1991], carbon concentration 0.34% (by weight), measured at 9.9 GHz.

Table A-4. *Electrical properties of simulated microwave absorbers.*

low longitudinal impedance at the beam modulation frequency and harmonics to minimize power loss. The gap should be as narrow as possible consistent with the maximum surface electrical fields. Larger apertures reduce the transverse impedances, but increase the core volume. An aperture of 5 cm was chosen as a base design. This allows sufficient room for focusing magnets while meeting the desired core volume.

Microwave absorbing materials can be used to damp resonant modes. These materials have a complex permittivity and/or permeability. Table A-4 lists nominal values of the permittivities and permeabilities for the absorbing materials used in the numerical modeling. The permittivity and permeability are expressed as $\varepsilon = \varepsilon_o(\varepsilon' + i\varepsilon'')$ and $\mu = \mu_o(\mu\prime + i\mu\prime\prime)$, respectively. Here ε_o and μ_o are the free space permittivity and permeability.

Several geometries were considered for the gap design. Several variations to each geometry was made to study the effect on the gap impedance. Simulated material properties of the absorbers and insulator were varied over a nominal range as well as their location and size. POISSON was used to adjust the geometry for specific designs to achieve acceptable surface electrical fields. The induction cell design code AMOS [Deford 1989, Deford 1990b], was then used to determine the rf characteristics of the gap. AMOS simulations include power loss to absorbing material. All geometries considered met the transverse impedance requirement of $Z_{\perp 1} \leq 5,400\Omega/\mathrm{m}$ for transverse stability by aggressively damping all resonant modes.

A conventional design similar to the ETA II induction cell gap was chosen as the base design for engineering and costing purposes. Advantages of the conventional design include demonstrated performance on several induction accelerators, a ceramic insulator hidden from the electron beam thus lowering the susceptibility for arcing, and relatively low-surface electrical fields. The disadvantages are a large inner radius for the core and a low-gap capacitance. A

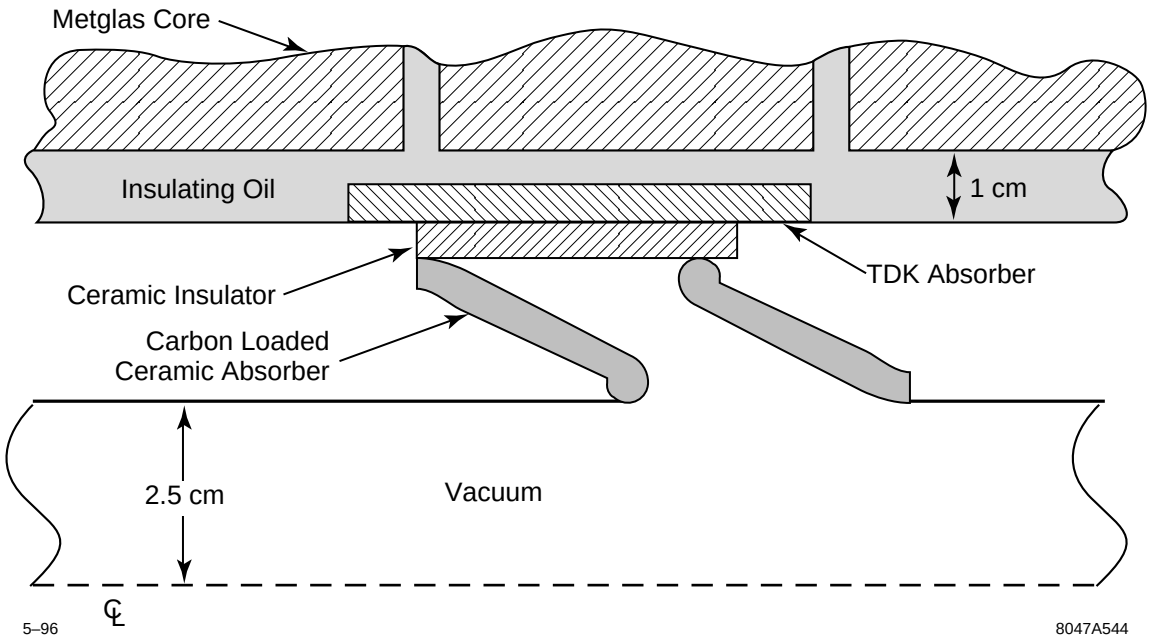

Figure A-12. *Schematic of a conventional design induction cell gap.*

low-gap capacitance is desired for fast rise times, but tends to be related to a high-longitudinal impedance which is undesirable. Figure A-12 displays a full-scale schematic of this design. Longitudinal and transverse impedances are shown in Figure A-13.

The most difficult design problem for all geometries studied was achieving a low-longitudinal impedance. The goal is for a power loss to the induction cells of $< 4\%$ of 360 MW per two-m module. This requires a $Z_{L0} < 2.4\Omega$ at 11.424 GHz. While impedance decreases rapidly above the cutoff frequency, the lowest Z_{L0} achieved thus far is about 10Ω at 11.4 GHz. Determining the longitudinal impedance accurately at 11.424 GHz is difficult. Analytical theory is available [Chattopadhyay 1990], but it is not clear that the quantitative accuracy is adequate. Numerically, the parameters of the test charge used, fineness of the grid, and the boundary conditions significantly impact the results. A cold test model needs to be fabricated and tested in the laboratory for a definitive answer.

A.4 TBNLC Engineering Design

A.4.1 TBNLC Systems Study Approach

The objective of the TBNLC system study was to assess the technical feasibility as well as the cost and efficiency of a TBA-based system. To achieve this goal, we felt that it was essential to be reasonably concrete. For this reason, our study specifically addressed a TBA power source for the NLC Upgrade considered by SLAC. The present thinking about the NLC is a 14.16-km active length linac with a center-of-mass energy of 500 GeV powered by X-band klystrons and rf pulse compression systems. This machine should be upgradeable to at least 1-TeV-c.m. Our study considered

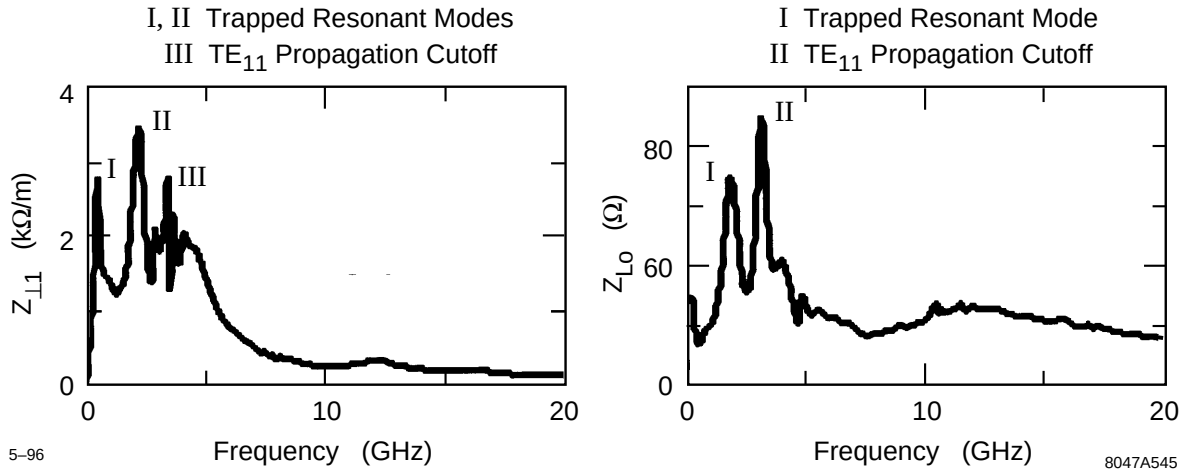

Figure A-13. *Longitudinal and transverse impedance of the induction cell gap.*

the TBA as a power source candidate for the 1-TeV version of the NLC. However, our modular architecture is directly applicable for a 1.5-TeV, ∼22-km NLC upgrade.

The engineering and costing efforts in the study drew heavily from recent work in Heavy Ion Fusion (HIF) [Hogan 1992]. The U.S. effort in HIF is based on the induction accelerator approach. Research activities in the past few years have centered around the Induction Linac Scaled Experiments [Fessenden 1992] (ILSE). Substantial engineering activities were committed to the ILSE CDR, and a 2-MV heavy-ion injector at full-driver scale was constructed and successfully operated in 1993. An engineering and costing study was performed recently for a recirculator version of the induction fusion driver.

A first engineering and costing exercise for the full TBNLC system was performed. The electrical design included all components starting from the AC power distribution system, to the DC power supplies, command resonant charging system, PFNs, and induction cores. Racks and installation, as well as instrumentation and control, were included in this exercise. The mechanical design and costing included details of the induction cells, rf structures, vacuum system, alignment, and utilities. Important aspects of the engineering design are summarized below.

A.4.2 Electrical Systems

A significant factor in the total efficiency of the TBNLC rf power source is the conversion efficiency of wall plug power into induction beam power. Figure A-14 is a schematic of an equivalent circuit of an induction accelerator cell. I_C is the core magnetizing current, I_B is the beam current, and I_N is any compensating network current. For optimum efficiency, I_N is minimized by designing the impedance of the PFN to match the nonlinear impedance of the induction core. The efficiency of an induction accelerator can approach 100% if the beam current is much greater than the current required to magnetize the transmission line (or autotransformer) which forms the induction cell. For example, the ATA induction cell required less than 1 kA of magnetizing current while accelerating a 10-kA beam by 250 keV for 70 ns; this corresponds to an induction cell efficiency of 91%.

The efficiency of an RK-TBA induction accelerator will depend on a number of factors. Beam transport dynamics will determine the size of the beam pipe and accelerating gradient. The rf power requirement will determine the pulse

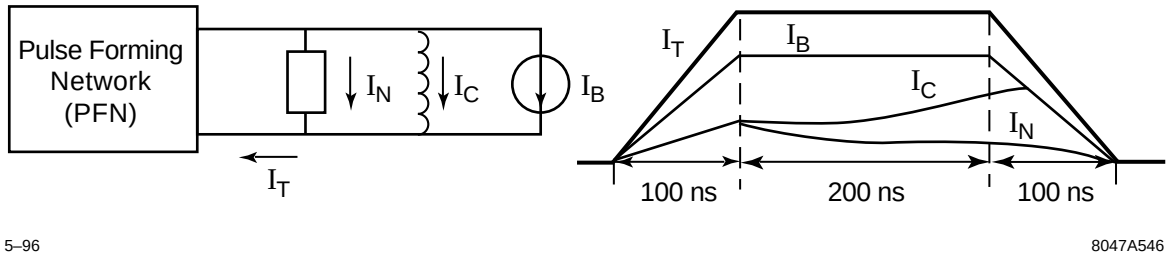

Figure A-14. *Equivalent circuit of an induction cell.*

duration, beam current, and repetition rate. Once these factors are set, the outer radius and flux swing of the core can be calculated from Equ. A.6.

Induction Accelerator Module

The linear induction accelerator can simply be described as multiple transmission line transformers driven in parallel by a pulse modulator which add energy to the electron beam in series as it passes through them. In order for the acceleration process to be efficient, the transformer or induction losses should be small compared to the energy imparted to the beam. Simply put, the transmission line current should be small compared to the beam current; therefore, the effective impedance of the transmission line, $Z_{\rm eff}$, should be greater than the beam impedance $Z_b = V_{\rm drive}/I_{\rm beam}$. In previously constructed induction accelerators, the high impedance is achieved by loading the transmission line with a ferri- or ferromagnetic material which is appropriate for the pulse duration. This material increases the impedance by $\sqrt{\mu/\varepsilon}$ and the electrical length by $\sqrt{\mu\varepsilon}$.

Typically, for induction accelerators with pulse durations of less than 100 ns, Ni-Zn ferrites have been used for the magnetic material due to their relative low saturation losses at very short pulse durations. However, the flux swing for Ni-Zn ferrite is only about one-fifth of that for Ni-Fe or METGLAS, and these materials are preferred for pulse durations of several hundred nanoseconds to microseconds. The optimization process in selecting the type of material and quantity is based on pulse duration, impedance, magnetizing losses, and economics. For the TBNLC design, the parameters are as follows:

$$I_{\rm beam} = 600\,{\rm A}\ , \quad V = 300\,{\rm kV}\ , \quad T = 300\,{\rm ns} \quad .$$

To satisfy the requirement that the effective impedance, $Z_{\rm eff}$, is greater than the beam impedance, $Z_{\rm beam}$ ~500 Ω, we can use the equation for a coaxial transmission line where $Z = \sqrt{\mu/\varepsilon}60ln(r_o/r_i)$. For ferrites, $200 < Z_{\rm eff} < 1000$, and for ferromagnetic materials $500 < Z_{\rm eff} < 5000$ depending on the type of material used and the magnetization rate. To satisfy the pulse duration requirements, the transmission line length should be about a single transit time. Since transit time is proportional to $\sqrt{\mu\varepsilon}$, for ferrites and ferromagnetic materials $T_{\rm eff} \simeq 100\ T_{\rm vac}$. The design of the transmission line (induction cell) must also ensure that no portion of the line is driven into saturation. This requirement dictates the outer radius of the line once the inner radius is determined by beam transport physics.

One of the most important considerations in the selection of a magnetic material for an induction cell is the actual losses during the magnetization pulse. Ferromagnetic materials such as nickel-iron have been available in thin ribbon cores since the late 50s when the first induction accelerator, the Astron, was constructed at Livermore by N.C. Christofilos. These iron-based alloys are very competitive in magnetic properties to the amorphous materials manufactured by Allied Signal and referred to as METGLAS. The time-dependent losses in ferromagnetic ribbons are typically explained in terms of a saturation wave which encircles the tape and proceeds toward the center at a rate

proportional to the applied voltage. The magnetic intensity required to change the state of magnetization is

$$H_a = H_c + (d^2/4\rho)(\Delta B/2B_s)(\Delta B/\Delta t) \quad , \tag{A.8}$$

where H_c is the DC anisotropy coercive field, d is the ribbon thickness and ρ is the resistivity. The energy density deposited in the tape during saturation is given by

$$E_L = H_c\Delta B + (d^2/4\rho)(\Delta B^2/2B_s)(\Delta B/\Delta t) \quad . \tag{A.9}$$

At high-magnetization rates, one can see that the losses are proportional to the thickness of ribbon squared and inversely to the resistivity. Since the ΔB of the iron alloys is similar to that of METGLAS, but the resistivity of METGLAS is three times that of the iron alloys, the ribbon thickness must be thinner in order for the losses to be comparable for METGLAS. The Ni-Fe alloys are manufactured by a rolling technique which yields a more uniform cross section while METGLAS alloys are manufactured by rapidly quenching a mixture of silicon and iron which remains amorphous. The quenching process leaves the ribbon surface rough compared to the rolled ribbon, hence it is more difficult to insulate and can yield an uneven cross section in the core winding process. Currently, the unannealed 20-μm METGLAS is wound into cores with 2.5-μm mylar between layers yielding a packing factor of 0.7 to 0.8 for a finished core. The iron alloys can be rolled into thinner ribbon than the METGLAS, and have produced lower overall losses. However, the manufacturing and winding process for METGLAS usually results in less expensive cores.

The induction cell will be driven directly by the modulator, *i.e.,* without step-up transformers. The modulator design is described below. To obtain 300 kV, 15 induction cells will be required. Since a standard width for the METGLAS is two inches, the TBNLC induction cell design was based on this width. The METGLAS alloy used for the design is 2714 AS. An example of a core test for the 2714 AS is shown in Figure A-15. The minimum amount of core material is realized when the flux swing approaches saturation. Minimizing the amount of magnetic material, however, does not lead to the most cost-effective design. A flux swing approaching saturation requires a very nonlinear drive current. This leads to a PFN which is difficult to design to achieve a flat voltage pulse. Furthermore, since the losses per unit volume are nearly proportional to ΔB^2, a better design is achieved by allowing a flux swing of less than one half of the saturation value. In this case, a ΔB of 1.0 T results in a dB/dt of 3.3 T/ μs and losses per unit volume of about 150 J/m^3. The inner radius of the induction cell is dictated by beam transport physics and is 4.5 cm for our TBNLC design.

Equation A.6 can be used to determine the required outer radius of the core. With ΔB = 1.0 T, Δt = 300 ns, G = 300 kV/ m, R_i = 4.5 cm, core occupancy $\eta_c = 0.75$, and a packing factor $F_p = 0.75$, we find that R_o = 20 cm and the volume of METGLAS is 4.5 10^{-3} m^3. The losses in joules are $E_L = (150\,\mathrm{J/\,m^3})$ (4.5 10^{-3} m^3) or about 0.68 J per core. The drive voltage for the induction core is 20 kV and the average current dissipated can be estimated from the losses, $E_L = VI_C\Delta t$, or from Eq. A.7. For a 300-ns pulse, the average magnetizing current or drive current of the core I_C is 117 A. The magnetizing current actually has a nonlinear component, as seen in Figure A-15, which reflects the characteristics of the B-H loop. The total drive current (I_T) from the PFN is the sum of the beam current (I_B), the core current (I_C), and the compensation network current (I_N), which for our design is approximately $I_T = I_B + I_C + I_N = (600 + 117 + 33)$ A $= 750$, yielding a core efficiency of 600/750 = 80%.

Line Modulator

The modest repetition rate (120 Hz) and current rise time (100 ns) envisioned for the NLC permits the use of a simple and cost-effective thyratron-driven modulator. For the TBNLC, each induction cell is comprised of five cores individually driven at 20 kV. Driving at this voltage level avoids any step-up transformers and can be generated directly by a thyratron with a 40-kV charging voltage on the PFN. After a preliminary search, the English Electric Valve (EEV) CX1525A appears to be an excellent thyratron for our application. It is a two-gap, deuterium-filled thyratron with a

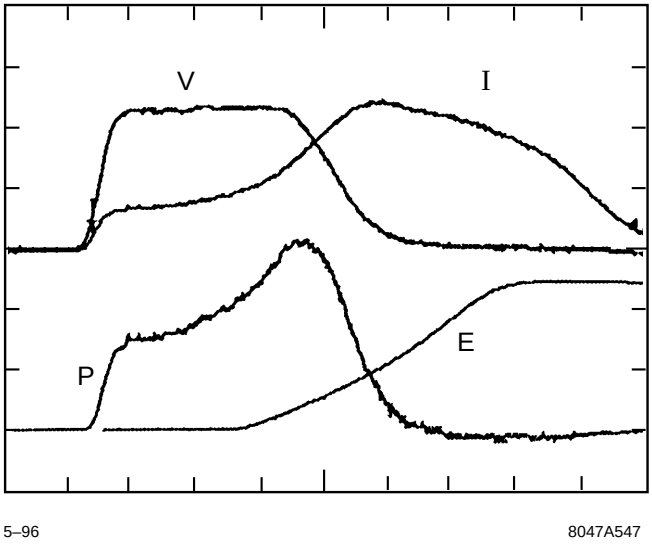

Figure A-15. *Oscilloscope traces for pulsed METGLAS 2714 AS core with cross section of 12.7 cm^2, volume of 450 cm^3, and packing factor = 0.7. Time scale = 100 ns/div. V is applied voltage (1 kV/div), I is current dissipated in core (50 A/div), P is power (VI, 50 kW/div), and E is energy (time integrated power, 20 mJ/div, 250 ns offset). Total energy dissipated = 47 mJ, or 150 J/m^3.*

voltage hold-off of 50 kV and capable of delivering 15 kA at 120-Hz repetition rate. Such a device would allow us to drive 15 cells for a total of 300 kV. A simplified schematic of the line modulator is shown in Figure A-16.

As shown in Figure A-15, the current drive to the cores is nonlinear, but a constant amplitude pulse can be generated, within bounds, simply by tapering the impedance of the PFN stages. The PFN will consist of many coupled L-C stages with impedances adjusted to temporally match the induction core impedance. The PFN charging current flows through the induction core, resetting the core prior to the next acceleration cycle. The combination of 2714AS METGLAS cores and the thyratron-driven modulators will result in a conversion efficiency of wall-plug power to cell power of 62%.

Command Resonant Charging and Core Reset

During the energy delivery cycle to the beam, the magnetic core requires a large magnetic intensity to swing 1.0 T in 300 ns. After the pulse is over, the magnetic intensity is reduced to zero, but the flux density has a remnant field, B_r. In order for the core to be useful on the next forward or energy delivery cycle, a reversed magnetic intensity or reset must be applied to the core. The reverse magnetic intensity, however, is much smaller than the forward one, since the rate of demagnetization can be much lower or $\Delta I_{\rm reset} \ll \Delta I_{\rm forward}$. By applying the reset current, the flux density is returned to $-B_r$, and the core is ready for the next forward or acceleration pulse. The PFN must be recharged after each forward cycle. The charging process occurs when the command resonant charging (CRC) switch is closed and delivers a half-sine current pulse from the large energy storage capacitor, C_E, to the PFN capacitors. It can be seen from Figure A-16 that the charging current for the PFN flows through the induction cells in the proper direction to reset them. By arranging the impedance and charge time, the proper reset current can be delivered to the cores at the same time that the PFN is being recharged. The reverse magnetic intensity required for reset is about 25 A/m. This is equivalent to about 24 A per core or 360 A for a complete induction module. Since one CRC charges six line modulators, a total of 2.2 kA are required. At the charging voltage of 40 kV, the reset/recharge impedance is 40 kV/2.2 kA= 18.2 Ω. The total

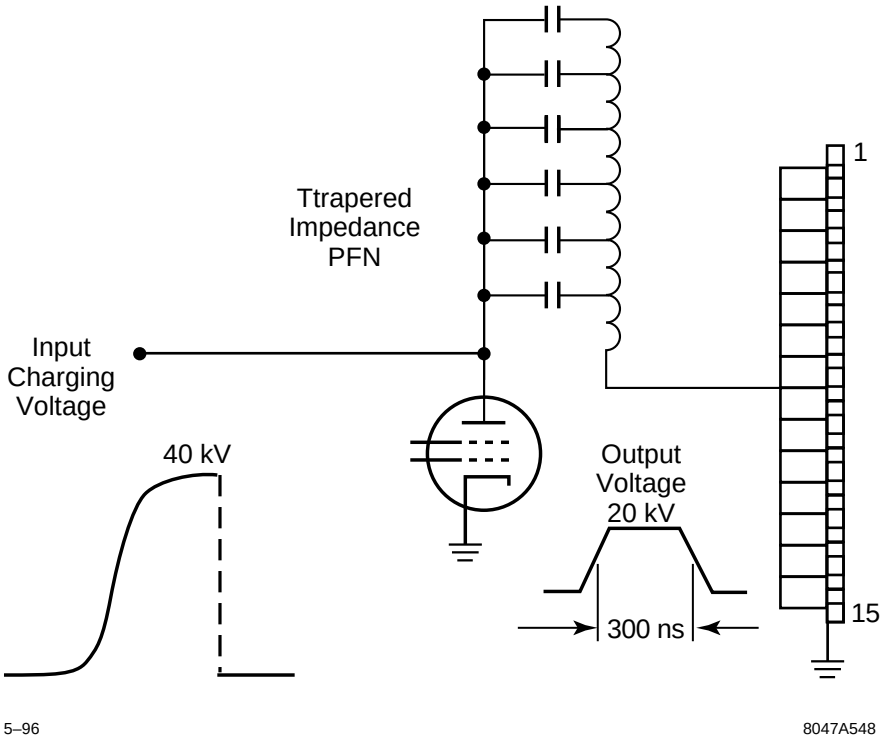

Figure A-16. *Simplified schematic of the line modulator. The PFN will have the same temporal impedance as the nonlinear magnetic core of the induction cells.*

capacitance (C_T) of six line modulators is 0.66 μF. The resonant impedance, $Z_r = \pi\sqrt{L_T/C_T}$, requires a charging inductor $L_T = 225\ \mu H$. Hence, the reset/recharge period $T_R = \pi\sqrt{L_T C_T} = 38\ \mu s$.

Efficiency of Induction Accelerator Components

The power conditioning system for the low-energy accelerator has energy losses associated with each major component from the utilities feeding the DC power supply to the induction cell coupling to the electron beam. These losses will be described in reverse order beginning with the induction core to beam coupling as shown on Figure A-17.

The acceleration voltage pulse is shown in Figure A-16. It has a rise time and a falltime of 100 ns with 200-ns flattop. There is no useful energy generated during the falltime, hence, this is lost. The energy during the rise and fall of the pulse is:

$$E_r = \int_o^{t_1} V \cdot I \ \ dt \quad , \tag{A.10}$$

where $V = V_o(10^7 t)$ and $I = I_o(10^7 t)$. By taking the integral, we find that $E_r = 10^{14} V_o I_o (t^3/3) = 0.4$ J, while the total energy during the pulse is $E_t = 3.2$ J . The induction core to beam efficiency is then $\varepsilon_b = 2.8/3.2 = 87.5\%$.

The magnetic materials losses have been discussed above. The magnetization current for each induction core was estimated to be 117 A. Another 33 A of current was added for compensation network at the core for a total current drive of 750 A. Hence, the efficiency of the induction accelerator cell is $\varepsilon_c = 600/750 = 80\%$.

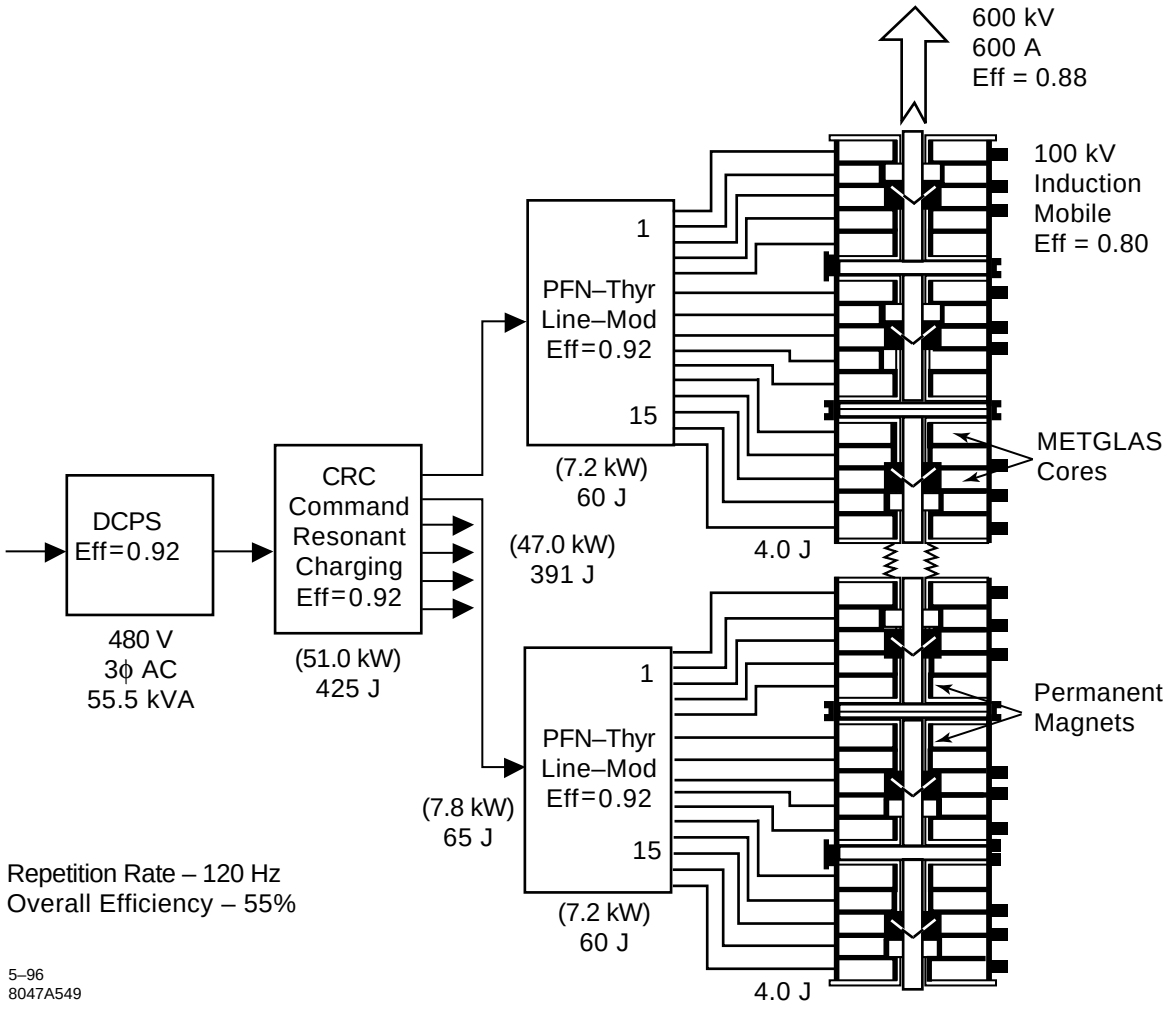

Figure A-17. *Schematic of the power conditioning system for a two-m RK module section.*

As previously discussed, the modulator consists of an impedance-tapered PFN matched to the drive required by the magnetic material, METGLAS 2714 AS. The efficiency is calculated by including the thyratron dissipation, filament, grid bias, keep-alive, and the pulse-shaping resistors losses. The modulator losses add up to nearly one kilowatt. At 120-Hz operation, the total power input has been calculated at 10.6 kW which yields an efficiency ε_m = 92%.

The line modulator is charged by a solid-state CRC system. The CRC generates a $1-\cos\omega t$-voltage waveform which charges the PFN. The current in the CRC is a half-sinusoid which flows through the induction cells in the resetting direction while the PFN is being charged. The losses for the CRC include the inductor mode-damping resistors, the solid-state switch losses, the trigger generator, and the de$Q$ing or regulation system if the DC power supply has insufficient regulation. The overall efficiency of the CRC is calculated to be $\varepsilon_{ch} = 92\%$.

The 20-kV DC power supply will be a conventional 60-Hz, 3-phase, full-wave rectifier with filter. It is projected that the power factor for the power supply will be 0.9 for an efficiency $\epsilon_{\rm ps} = 92\%$.

The overall efficiency of the induction accelerator from the utilities to the electron beam which drives the RK is the product of the individual component efficiencies or $\varepsilon_o = 55\%$.

A.4.3 Mechanical Systems

Module Design and Fabrication

The TBA consists of essentially 50 identical RKs stacked end-to-end to form the 15-km overall length. Each of the 300-m-long RKs contain 150 identical extraction and reacceleration sections. These 2-m-long sections are referred to as RK modules. A schematic of a 2-m RK module is shown in Figure A-3. An RK module consists of six identical induction modules and one extraction cavity. Each 300-m RK contains 900 modules and the complete TBNLC will contain 45,000 identical modules.

In the design of the module a large effort was made to keep the geometry of individual parts simple and amenable to mass production. This basically requires designing so that a minimum amount of material has to be removed during part fabrication. Drilling, tapping, and machining of small slots are kept to a minimum as these operations are relatively slow operations. All metal parts are made of 304 stainless steel alloy. Advances in modern stainless steel alloys enable significantly greater cutting speeds. Metal stamping and molding of plastic parts are used to further reduce part costs.

The module assembly relies on brazing and welding. The beam pipe assembly uses six brazed joints. Use of simple fixtures to align the stacked parts and brazing in large batches keeps the time and cost per assembly very low as compared to other methods of assemblies. The final housing assembly is done with an inner and outer weld at each end plate. Automatic welding machines make this a quick and reliable operation.

Core Winding

An individual core winding is made by winding approximately 4700 turns of METGLAS ribbon onto a winding mandrel. The ribbon is 20-μm thick and 51-mm wide. A thin layer of insulation will be dipped or sprayed onto the METGLAS during the winding process to provide adequate resistance to eddy currents between turns. The average voltage between turns is 5. This insulation will replace the thin mylar ribbon presently used to provide core interturn insulation. The mylar ribbon overhangs the core edges and presents a serious problem to edge-cooling the cores. A technique being developed at LBNL uses a thin layer of epoxy, dipped or sprayed on, and then dusted with alumina grit to form a tough interlayer insulation. The epoxy additionally binds the METGLAS layers together to form a rigid self-supporting core.

Core Cooling

Heat generation within the cores will be about 300 W per core. Cooling of the core windings is accomplished by circulating oil through the module housing. Oil flows in at one end of the module housing and flows out at the other end on the opposite side. This causes the oil to flow transversely in the gaps between the cores. Spacers around the outside diameter of the cores prevent oil from flowing around the outside of the cores. Only moderate oil flow rates are required and as a result there is a low-pressure drop between supply and return manifolds. For a flow rate of 27°C oil at 1.25 gpm through the module, the maximum temperature for all the cores is about 60° C on the down-stream side. Quadrupling of the oil flow rate will drop the core temperature by about 13° C. Core temperatures in this range

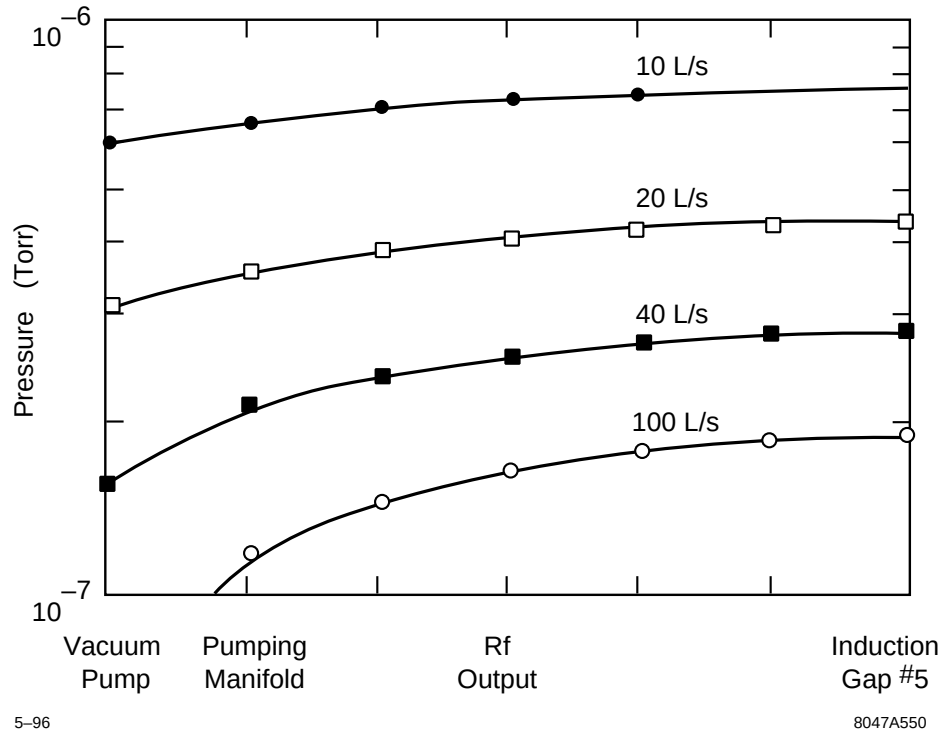

Figure A-18. *Gas pressure distribution within the 2-m module.*

are acceptable; magnetic properties are not affected, thermal stresses are minimal since the core remains at a nearly uniform temperature, and temperature limits on the plastic materials within the module are not approached.

Development of an interlayer insulation to replace the presently used mylar tape is critical for the cooling of the cores. Presently used mylar tape overhangs the edges and largely blocks the transfer of heat from the METGLAS to the oil. As described in Section A.4.3, "Core Winding", alternative interlayer insulations are being developed.

Vacuum System

The accelerator will be pumped in two places in each 2-m module. Pumping will occur at the start of each module on each side of the extraction cavity. There is a 2-cm gap between modules at these points which permits good pumping conductance to a standard mounting flange. The two ports are manifolded together to a single ion vacuum pump. The total gas load per cell block is about 8×10^{-7} Torr-ℓ/s. For this geometry, the pressure between the pump and the rf output structure entrance is calculated for several pumping speeds and results are shown in Figure A-18. In this figure, Induction Gap #5 refers to the most distant induction cell from a pumping manifold. If a 20-ℓ/ s pump is chosen, the pressure at the rf output structure entrance will be about 5×10^{-7} Torr.

An inline gate valve between every fourth 2-m module will enable isolation of small sections of the accelerator. In each of these four 2-m modules a right-angle gate valve will be used to enable initial pump down with a portable turbomolecular pumping station.

Moderate pressure levels within the linac will enable some of the more costly cleaning methods used on ultrahigh vacuum systems to be avoided. This will be an unbaked system with a base pressure in the 10^{-7}-Torr range. Systems of this type are generally cleaned by chemical or glow discharge cleaning techniques and perhaps a bake at low temperatures.

Assembly and Alignment

Alignment requirements for the TBA can be achieved using standard fabrication, assembly, and alignment techniques. The centerlines of the 2-m modules will be aligned to within 0.1 mm of their nearest neighbor's centerlines. A gradual accumulation of position errors between successive 2-m modules will occur, and will result in the accelerator not being straight. This is acceptable as long as these bends are not extreme and occur gradually over many half-lattice periods.

Six induction cells will be supported and aligned accurately with respect to one another on one strongback support beam. As shown in Figure A-4, each cell has two quadrupole assemblies. The permanent magnets will be sorted by field strength to optimize paring in the quadrupole assemblies. The magnets will then be bonded into the assemblies that are held in place by the cell end plates. Quadrupole correction coils will be used to minimize the field errors, instead of attempting to adjust the magnetic center of individual quadrupole assemblies. These procedures will require the permanent magnets to be positioned with a tolerance of 0.1 mm within the 2-m modules. The required tolerance for each step of the assembly will be 0.05 mm. This will ensure that the quadrupole assemblies are well centered with respect to the outside diameter of the cell housing end plates.

The support mounts for all the induction cells on each strongback beam will be positioned and aligned accurately during fabrication of the beam. Mounts for the modules will be welded, machined, and then ground to the required precision. As a result, within each 2-m module, the 12 magnetic quadrupoles will be aligned to the required precision when the modules are assembled onto the beam. There will be no provision made for adjusting the position of magnets within a 2-m module with respect to each other on the beam.

There will be an X and Y set of fiducials at each end of the beam. After the installation of the 2-m modules onto the beam line, a precise measuring fixture will be used to adjust the position of each fiducial accurately with respect to the center of the last quadrupole at each end of the beam. It is desirable to make the fiducials reflect the position of the end quadrupoles rather than some average position for each 2-m section. This will enable the last quadrupole on one beam to be aligned well to the first quadrupole on the next beam.

As successive 2-m modules are installed, they will be aligned using the fiducials to a straight-line reference system. Each module is supported and articulated using a six-strut system. This enables the section to be moved easily and with precision in all six degrees of motion. The straight-line reference system will be able to accurately detect the position of each fiducial. The 2-m module is then articulated to bring the fiducials into a straight line.

A stretched wire can be used with optical sensors to detect the position of the wire. A laser-based system can be used although a pipe under vacuum is necessary for the light. A series of overlapping straight reference lines will be needed to form the entire 300-m length.

A.5 RTA Test Facility

We are constructing a prototype RK-TBA rf power source to verify the analysis of the TBNLC system study. This prototype, called the RTA, will be located at LBNL. All major components of the TBNLC rf power source will be tested. However, due to fiscal constraints, the prototype will have only 8 rf output structures, with a possible upgrade

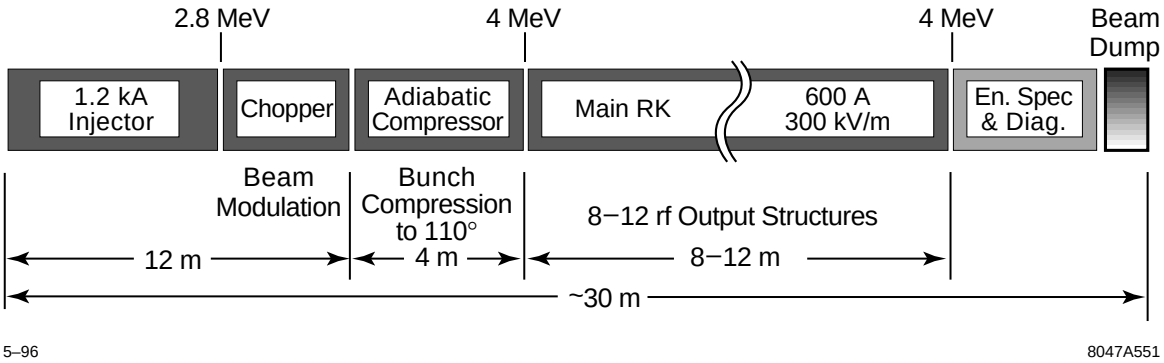

Figure A-19. *Schematic of the RTA showing major components.*

to 12, instead of the 150 envisioned for the TBNLC. A schematic of the RTA is shown in Figure A-19. Table A-5 lists pertinent parameters for the RTA and TBNLC power source.

The more important issues to be addressed by the RTA are efficiency, longitudinal dynamics, beam stability, emittance preservation, and rf power quality. Efficiency can be separated into the conversion efficiency of wall plug power into beam power and beam power into rf power. The conversion of wall plug power into beam power is described in Section A.5.1 and can be fully measured in the RTA.

High conversion efficiency of beam-to-rf power can be obtained in a system with a large number of output structures. For the TBNLC rf power source, the number of output structures will be limited by beam stability and transport issues. The direct study of beam dynamics issues involving the beam transport through many tens of output structures will not be possible with the prototype. However, the reduced beam energy in the extraction section of the prototype permits the observation of almost an entire synchrotron period. This will be sufficient to allow the beam to approach a steady state condition that can then be extrapolated to a full-scale system with high confidence. The verification of computer simulations used to model the beam dynamics in the TBNLC system study will be a high priority. Beam dynamics issues related to transverse modulation, misalignment of magnetic focusing systems, and adiabatic compression, *e.g.*, emittance growth and corkscrew motion, can be adequately studied.

A.5.1 Induction Cores and Pulsed-Power System

For our prototype, we will use two different pulsed-power systems. The adiabatic compressor and extraction sections will use induction modules and a pulsed-power system very similar to those described in Section A.4.2 and the TBNLC system study. The primary difference is that each induction module is comprised of three individually driven cores. The cores are still driven at 20 kV by a thyratron charging a multistage PFN. This part of the experiment will be used to verify the efficiency, technical aspects, and cost of the induction modules in the TBNLC.

As described below, the injector is comprised of modified versions of existing equipment. Here, the issue is generating the required volt-seconds within the geometrical constraints of these components. The magnetic material will be 2605 SC METGLAS to maximize flux swing, and the cores in each module will be driven as a single unit to maximize the available cross-sectional area. Driving multiple cores will require the use of a step-up transformer to deliver the required 80–100 kV per cell.

Parameter	RTA	TBNLC
Pulse		
Duration	200 ns	300 ns
Rise Time	50 ns	100 ns
Current:		
Pre-modulation	1,200 A	1,200 A
Extraction section	600 A DC	600 A DC
	1,100 A rf	1,150 A rf
Beam energy:		
Injector	1 MeV	1 MeV
Modulator	2.8 MeV	2.5 MeV
Extraction	4.0 MeV	10.0 MeV
Bunch compression	240°-110°	240°-70°
Extraction section		
PPM quadrupoles:		
Betatron period	1 m	2 m
Lattice period	20 cm	33.3 cm
Phase advance	72°	60°
Occupancy	0.5	0.48
Pole-tip field	870 G	812 G
Beam diameter	8 mm	4 mm
Rf power:		
Frequency	11.4 GHz	11.4 GHz
Power/structure	180 MW	360 MW
Structures	SW & TW	3 cell TW
Output spacing	1 m	2 m

Table A-5. *Comparison between RTA and the TBNLC.*

A.5.2 Injector: Gun and Accelerator Sections

Two main goals of the injector design are minimizing electrical field stresses in the gun and realizing the lowest possible emittance growth. The gun and accelerator section comprising the injector, will be modifications of the SNOWTRON induction injector and induction cells from ETA II. Modifications include replacement of the original ferrite cores with METGLAS and a new mechanical alignment system. The present electrode package will be used during initial testing. However, a new electrode package and larger dispenser cathode are required to produce the desired 1.2-kA, 1-MeV beam. The solenoidal field configuration must be optimized for the injector to control the beam radius while minimizing emittance growth. The design goal for the experiment is for a radius < 5 mm and $\epsilon_N < 250\pi$-mm-mr at the chopper entrance.

Alignment of the focusing solenoids is critical to avoid corkscrew motion and emittance growth in the injector. A stretched wire alignment scheme [Griffith 1990] will be used to determine the offset of the solenoid's magnetic axis from a reference mechanical axis for each cell. From past experience, the resolution of this alignment scheme to offset errors is approximately ± 0.05 mm. For offset errors of more than 0.5 mm, the solenoids will be repositioned in the cells. Offset errors of less than 0.5 mm will be recorded, but the solenoids will not be repositioned. A 0.5 mm

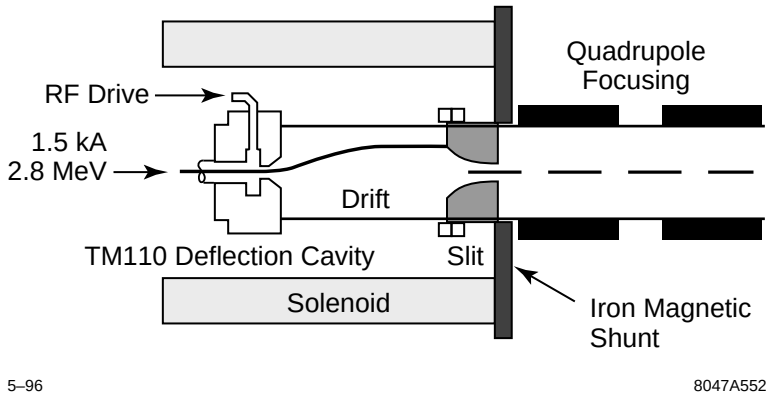

Figure A-20. *Schematic of the beam modulator (chopper).*

represents the maximum one induction cell can be mechanically offset from an adjacent cell to achieve magnetic alignment. Each cell also contains a steering (sine/cosine) coil to correct for tilt errors. The required tilt correction will also be determined. The entire alignment will be performed in a precision mill with tolerance on the order of tenths of a mil. A fiduciary will be placed on the outer case of the cell to permit alignment of the magnetic axis when the cells are mounted on the strongback. With this procedure, we expect solenoid offset errors of less than ± 0.08 mm and negligible tilt errors.

Experience operating the ETA II accelerator has shown that careful alignment of the solenoids is not sufficient to reduce the amplitude of the corkscrew motion [Allen 1991] to 0.5 mm desired for the RTA injector. Individual adjustments for the induction cells will permit improved solenoid alignment in the RTA. However, we anticipate using a time-independent steering algorithm [Chen 1992] developed for ETA II to control steering coils on the solenoids. This algorithm corrects for the Fourier component at the cyclotron wavelength of the field error, and led to an order of magnitude reduction in the corkscrew amplitude of the ETA II beam.

A.5.3 Chopper: Beam Modulation

A transverse chopping technique will be used to modulate the beam. The modulator section of the Choppertron, a 11.4-GHz rf generator, will be refurbished for this purpose. A schematic of the modulator is shown in Figure A-20. The solenoidal field immersed incoming electron beam is deflected in the horizontal plane by a 5.7-GHz TM_{110} deflection cavity causing the beam to describe semihelical trajectories along the drift space. The beam scans in a vertical plane across an on-axis aperture placed a quarter betatron wavelength after the deflection cavity. Thus, the 5.7-GHz spatially-modulated DC beam incident on the aperture becomes a phase-coherent, amplitude-modulated beam at 11.4 GHz.

The desired bunch length, peak current, and energy for the drive beam in the extraction section of the prototype is respectively 110°, 600 A, and 4 MeV. Such a train of bunches could be generated by directly chopping the unmodulated beam. However, considerations of efficiency (70% of the beam would be lost) and practical feasibility (we expect approximately 1.2 kA of peak current from the injector) require that we do not fully modulate the beam by chopping. Our intent is to chop the beam at an energy of 2.8 MeV into bunches of approximately 240°. An adiabatic compressor section will be used to further bunch and accelerate the beam.

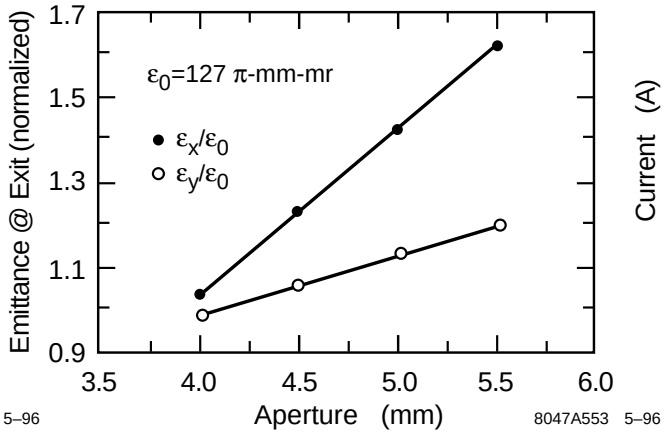

Figure A-21. *Emittance growth as a function of aperture size*

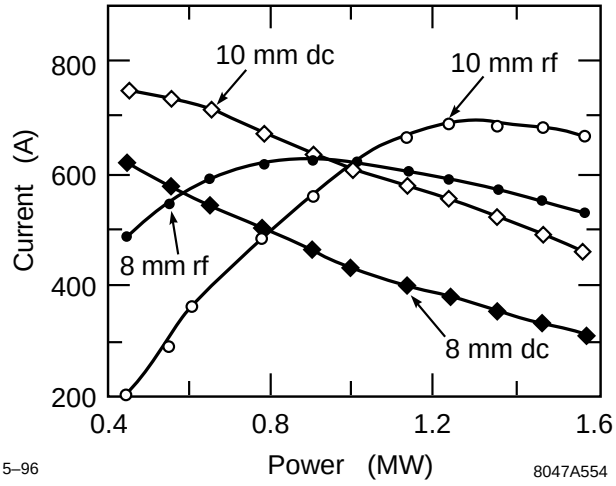

Figure A-22. *The DC and rf (11.4-GHz) current components as a function of drive power to the deflection cavity for two apertures.*

Designs of chopper systems have been extensively analyzed [Haimson 1965, Haimson 1970], and the original Choppertron was optimized for operation with the ETA II induction beam. The intent for the prototype experiment is to limit modifications of the modulator section of the Choppertron to adjustments in the drift length and the chopping slit aperture size. It is desirable for the radius of the beam to remain relatively constant in the chopper. For a given beam energy, current, and emittance, the radius is determined by the solenoidal field. Once the solenoidal field is determined for the desired beam radius, the drift section length is also fixed. The maximum deflection amplitude at the aperture is determined by the transverse momentum imparted to the beam by the deflection cavity. The deflection amplitude and chopping slit aperture determine the emittance growth and the modulated beam's characteristics.

A series of simulations were performed with the relativistic klystron design code RKS to determine the optimum deflection and aperture. Results are shown in Figures A-21 and A-22. The beam was assumed to be cylindrical with a maximum radius of 3.6 mm, waterbag distribution, and normalized, rms emittance (ε_x and ε_y) of 127 π-mm-mr at the chopper entrance. In Figure A-21, the emittance has been normalized with respect to the initial value. The emittance represents the area in trace space for all the particles within a 360° rf bunch length. The emittance increases with the chopping slit aperture as the simulations cover the range where a substantial current loss occurs on the aperture. Thus, the beam has been deflected to fill the acceptance of the aperture. The difference between the x and y emittances is due to the deflection in a single plane. In the simulations, x represents the horizontal plane.

Considering only the increase in emittance, it would appear that the smaller aperture is better. However, as shown in Figure A-22, the amount of current contained in a 240° bunch length is substantially reduced as the chopping slit aperture is reduced. We require at least 600 A of the initial DC current to remain in this bunch length for the adiabatic compressor section. To allow for current losses during the adiabatic compression, 660 A is a practical limit. Also, the beam must be sufficiently modulated for the idler cavities in the adiabatic compressor to function. The rf current component (modulation) initially increases with drive power, as shown in Figure A-22, with a decrease in DC current. The design goal of the chopper is to generate a 240° rf bucket containing 600 A that can be captured and bunched by the adiabatic compressor, with minimum emittance growth. Maximizing the rf current at the exit of the chopper will not optimize emittance growth with respect to DC current in the rf bucket. A 10-mm aperture at a drive power of about 0.8 MW produces a satisfactory modulation for growth in emittance, although further studies are required for an optimum design. Future simulations will use the results of EGUN simulations for the initial beam characteristics.

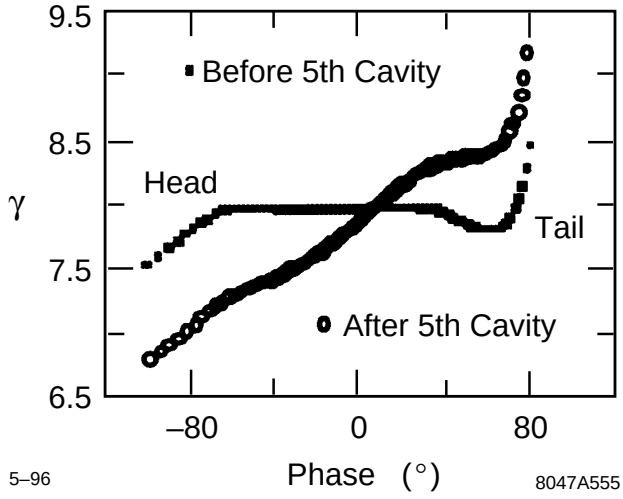

Figure A-23. *Simulations of longitudinal phase space before and after the 5th idler cavity.*

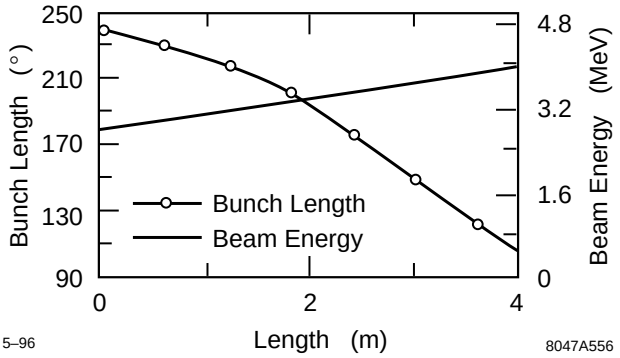

Figure A-24. *Simulations of adiabatic compressor effect on bunch compression and beam energy.*

A.5.4 Adiabatic Compressor

Adiabatic compression is used to achieve the desired beam characteristics at the entrance of the extraction section. In the adiabatic compressor, the bunch length is reduced from 240° to 110° with SW idler cavities while the beam is accelerated to an energy of 4 MeV. The accelerating gradient of the induction cells (300 kV/m) sets the minimum length of the adiabatic compressor to 4 m. Extensive 1-D numerical studies have been performed to determine the most efficient scheme for accomplishing this: The present design uses seven idler cavities appropriately spaced and detuned to progressively bunch the beam. The idler cavity has a resonant frequency higher than the drive frequency. The rf field in the cavity, excited by the beam, places itself at 90° with respect to the rf bucket. This leads to a loss of energy for electrons towards the front of the rf bucket, and a gain for those in the back.

The bunching effect of the idler cavity is illustrated in Figure A-23. As the beam drifts between the idler cavities, electrons in the tail of the rf bucket have a greater velocity leading to increased bunching. At the same time, space charge forces will increase the energy of electrons at the head of the bunch with respect to the tail slowing the bunching process. Appropriately designing and spacing the idler cavities can eventually bunch the bucket to the desired length. Table A-6 summarizes the important parameters of the adiabatic compressor, and Figure A-24 shows the overall effect on the beam.

A.5.5 RF Power Extraction

After leaving the adiabatic compressor, the beam enters the main RTA where power is extracted. Here the beam energy is periodically converted into rf energy (via output cavities) and then restored to its initial value (via induction modules). Stable propagation of the rf bucket traveling through many resonant cavities and achievable power output extraction have been studied numerically. Space-charge effects and energy spreads due to rf fields in the output structures tend to debunch the beam as it traverses the main RTA. To counteract this effect, inductively detuned output structures are used.

Cavity	Position (m)	Bunch length (°)	Beam E_k (MeV)	Resonant freq. (gHz)
1	0.0	240	2.8	11.82
2	0.6	229.7	2.98	11.82
3	1.2	217.9	3.17	11.82
4	1.8	201.7	3.36	11.74
5	2.4	177.6	3.53	11.74
6	3.0	148.6	3.69	11.74
7	3.6	122.0	3.85	11.74
exit	4.0	105.5	4.00	

Table A-6. *Parameters of the adiabatic compressor.*

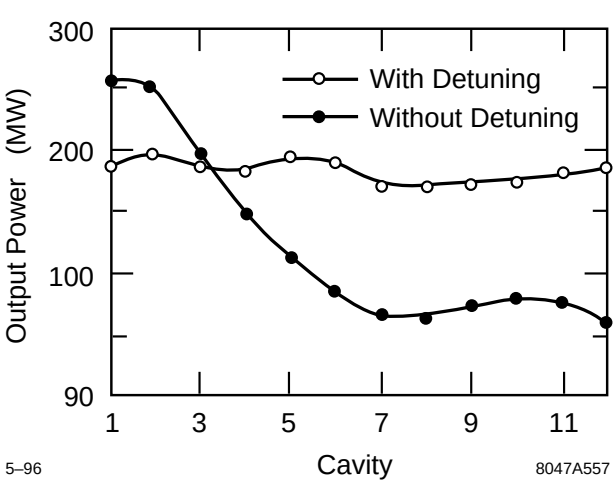

Figure A-25. *Simulations of the rf power generated per output, both with and without detuning of the output cavities.*

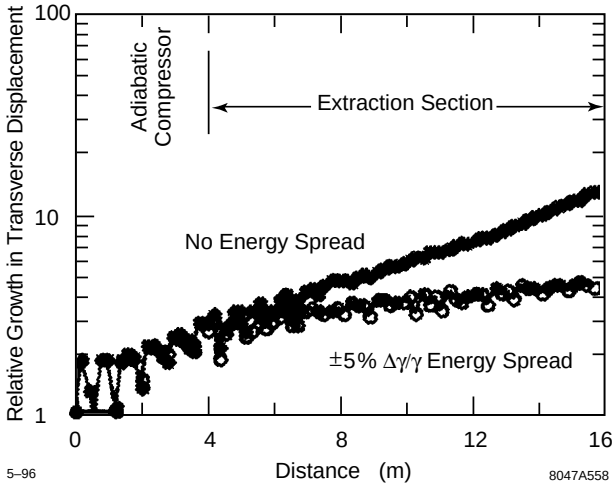

Figure A-26. *Simulations of growth in the transverse displacement of the beam centroid from deflection by HOMs in the induction cell.*

Both traveling wave (TW) and standing wave (SW) structures are being considered for the output structure design of the RTA. The TBNLC RK design used TW structures to reduce the surface fields associated with generating 360 MW per output. RTA is designed to generate 180 MW per output. Thus, inductively detuned SW cavities are a practical alternative. Furthermore, the RKS code is believed to incorrectly describe the radial beam dynamics for inductively detuned TW structures. [Giordano 1995] We have used SW cavities in our modeling to perform complete 2-D simulations and to validate the inductive detuning concept. The detuning concept for the SW output cavities is similar to that used in the adiabatic compressor cavities. The required detuning is also affected by the finite external Q of the cavities. Different cavities can have different Q values to optimize the output power and the bunching. The detuning mechanism is required for stable rf power production through the main RTA. See the simulation results in Figure A-25 Resonant frequency of the cavities was 11.566 GHz for this simulation.

A.5.6 Beam Dynamics Issues

Transverse instability of the beam due to the excitation of higher order modes (HOM) in the rf couplers and induction cell gaps is a serious issue for a long relativistic klystron. We do not anticipate beam loss due to the HOM excitation, but the effect should be measurable. The HOMs associated with three different components will predominate in the prototype. Fortunately, the frequency ranges do not overlap so that the effects can be studied separately.

The first is the approximately 300-MHz transverse mode in the accelerator induction cells. ETA II has operated with 3 kA of current through 60 induction cells of the same geometry, but with ferrite cores. The 20 accelerator cells in the RTA should not pose an instability problem with 1.2 kA of current, but it should be possible to detect weak beam oscillations at 300 MHz by using rf probes.

Of greater concern are the 60–80 prototype induction cells of the adiabatic compressor and extraction section. The transverse impedance of a cell is roughly proportional to the cell gap divided by the square of the beam-pipe radius. The transverse impedance of the smaller prototype cells is about four times that of the larger accelerator cells. Simulations of the growth in the transverse instability were performed using the OMICE code. Results are shown in Figure A-26. For the purpose of the simulation, the prototype cells were assumed to have the same characteristics as the TBNLC induction cells ($Z_{\perp 1} = 5,400\,\Omega/m, Q = 2$, resonant frequency = 3 GHz), the current was increased from 0 to 600 A in 50 ns, total pulse duration was 200 ns, and a step function offset was used as the excitation seed. One curve represents growth for a monoenergetic beam while the second has a $\pm 5\%$ energy spread over the rf bucket, imposed to illustrate the effect of Landau damping. The expected exponential growth is evident in Figure A-26, but well within the design goal of less than a factor of 100.

The third and most critical instability affecting transverse motion is caused by the rf output structures in the extraction section. Despite heavy damping of the structures and the effect of Landau damping, it was necessary to use the Betatron Node Scheme to suppress the transverse instability to a tolerable level for the TBNLC. Simulation results of the growth in the transverse instability through the extraction section are shown in Figure A-27. The rf characteristics of the three-cell traveling-wave output structures described in the TBNLC design study were used for the simulation ($Z_\perp/Q = 3\Omega$ per cell, dipole resonant frequency of 14 GHz, $Q = 10$ for the first and third cells and 3,500 for the second, and dipole phase advance of about $2\pi/3$). A monoenergetic beam with parameters the same as for the induction cell simulation was used for this simulation. A relative small change in the beam energy from that required for the Betatron Node Scheme can lead to substantial increase in the growth of the instability as indicated in Figure A-27. While the growth remains tolerable for both cases shown, the idler cavities in the adiabatic compressor require different transverse rf characteristics than the main RTA output cavities to avoid beam loss and/or adverse emittance growth. The difference in HOM power generated in the cavities is three orders of magnitude greater after 12 cavities when not operating at the energy for the Betatron Node Scheme. A measurement of the HOM component in the output power is expected to be sensitive to the effectiveness of the scheme.

Landau damping and the Betatron Node Scheme were both required for transverse stability in the TBNLC design. Neither are required for the operation of the RTA, but the effectiveness of both for a variety of operating parameters can be measured. The effect of the Betatron Node Scheme can be readily ascertained by measuring the HOM power generated in the output structure while rf loops distributed along the beam line can determine the effectiveness of Landau damping.

Longitudinal stability issues include both the rf bucket and the phase relationship between rf buckets. The rf bucket must remain appropriately bunched for stable rf current and power extraction as described in Section A.3.1. Simulation results of the rf power generated and bunching in the extraction section when the resonant frequency of all the detuned

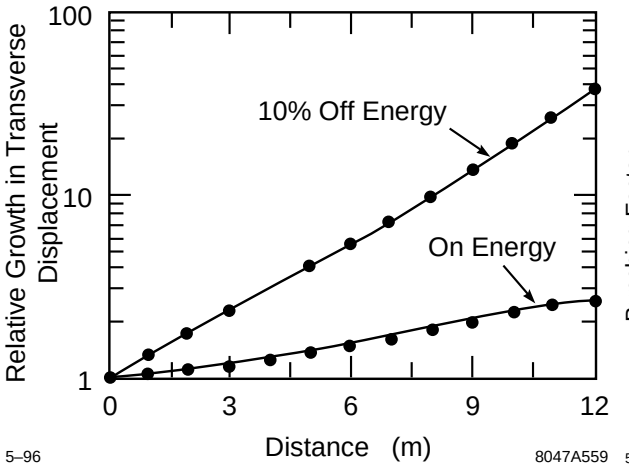

Figure A-27. *Simulations showing growth in the transverse displacement of the beam centroid from deflections by HOMs in the rf structures.*

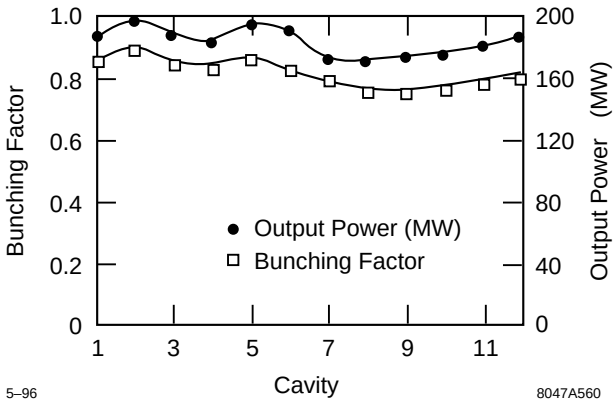

Figure A-28. *Evolution of bunching factor and power output in the main RTA with detuned rf output structures.*

output structures has been set to 11.566 GHz is shown in Figure A-28. The bunching factor is defined as:

$$b = \left| Re \left\{ \frac{1}{N} \sum_{n=1}^{N} e_n^{j\psi} \right\} \right| \quad , \tag{A.11}$$

where the sum is over all the electrons and ψ is the phase of the electron with respect to the center of the rf bucket. The relatively constant value of the bunching factor is a good indication of long term stability of the rf bucket.

The length of RTA is adequate for a meaningful measurement of the longitudinal beam dynamics involved in the detuning of the output structures to maintain the rf bucket. The synchrotron wavelength can be expressed as:

$$\lambda_s = 2\pi \left(\frac{\omega}{c\gamma^3} \frac{d\gamma}{dz} \right)^{-\frac{1}{2}} \quad . \tag{A.12}$$

At 4 MeV, accelerating gradient of 300 kV/ m, and 11.4 GHz, λ_s is ≈14 m. Numerical sensitivity studies indicate that rf output power is insensitive to energy variation and shows small variations ($< 4\%$) for current variations of $\pm 1\%$. The variations were imposed for the flattop portion of the beam pulse. Phase stability is not appreciably effected by current variations of less than $\pm 1\%$. However, phase sensitivity leads to a severe requirement on the average (head-to-tail) energy variation for the flat-top portion of the beam pulse. Phase variations are well modeled by the following first-order formula:

$$\frac{\Delta\psi}{\Delta z} = \frac{k}{\overline{\gamma}^3} \Delta\gamma \quad , \tag{A.13}$$

where $\Delta\psi$ is phase variation, $\Delta\gamma$ is head-to-tail energy variation over the pulse length, k is the free space wave number, and $\overline{\gamma}$ is the average beam energy. With the RTA parameters, assuming that field phase variation should not exceed $\pm 5^\circ$, the required pulse energy flatness (flattop) is estimated to be $\pm 0.3\%$ for an 8-m extraction section.

Beam emittance is an important parameter for the RTA. After the chopper, the focusing system is comprised of permanent quadrupole magnets. The ppm quadrupole focusing is important in the TBNLC design for cost and efficiency reasons. For the RTA, mechanical design constraints and the experimental goal of studying the Betatron Node Scheme require a pole field at a radius of 2 cm for the quadrupoles of about 870 gauss, a half-lattice period of

10 cm, occupancy factor of 0.5, and a phase advance of 72°. The normalized edge emittance must be no larger than 800 π-mm-mr to meet the design goal of an average beam radius (edge) in the extraction section of 4 mm.

Our goal is to limit the emittance growth in the injector from beam optics to a factor of three times the thermal source emittance of about 80 π-mm-mr (0.1 eV) for the cathode. The chopper is expected to increase the emittance by a factor of about 1.7. Thus it is very important to minimize sources of emittance growth such as nonzero magnetic flux at the cathode, magnet misalignments, solenoid to quadrupole matching, and higher order multipoles in the quadrupole magnets. The strong focusing used in the extraction section and the large beam energy spread will convert any transverse motion of the beam, *e.g.,* corkscrew motion or transverse instabilities, into an increase in effective emittance.

A.6 Conclusions

A preliminary design of an RK-TBA based rf power source for the NLC has been presented. The TBNLC system study focused on three major areas: (1) RK-TBA physics, (2) RK-TBA engineering and (3) RK-TBA costing. Here we have described the more important results related to physics and engineering from that study. In addition, we have described an experimental program to construct and test a prototype rf power source based on this design. The description of this program emphasized a number of the RK-TBA engineering issues studied in the TBNLC system study.

The issue of an economical and efficient rf power source is central to the development of future linear colliders. While the induction linac based TBA is known to have the potential for very high efficiency, research support received to date has been somewhat limited. General concerns about the TBA concept as a realizable power source include:

- The induction linac technology is not as mature as existing rf-klystron technology.
- The TBA beam dynamics, particularly BBU, is difficult.
- Induction linacs are perceived to be very expensive.

The objectives of the RK-TBA research program at LBNL and LNLL were motivated by these concerns.

In regards to the cost issue, past cost estimates were based on induction linacs built for other applications (short pulse, high-repetition rate, high current). Our belief has been that the induction linac design ought to be optimized for the specific mission. Hence, the TBNLC system study was specifically directed towards an rf power source suitable for the NLC. Likewise, the experimental program is developing a prototype rf power source that is suitable for powering the NLCTA.

Since cost is, and will be, a key issue for future colliders, we feel that it is essential to have a believable cost estimate. The only way to have a believable cost is to carry the engineering study to sufficient details to make a bottom-up estimate possible. We have tried to estimate cost for fabrication and assembly on the basis of engineering drawings and proposed mass-production procedures. For the induction modules, a major component of the machine, we have sent out for external bids for various parts, to cross-check our own estimates. Our estimate, for approximately ten different items, agreed with external quotes to a few percent on the total. All components are based on known technology, with relatively well-known costs. Hence for the engineering design proposed, we believe that our cost estimate is realistic.

Similarly, the efficiency estimate for our pulse power design is based on well-known numbers with today's technology. We have not made any extrapolations for possible future innovations. We might note here that as we have done more testing in the experimental program, the 40% number quoted in the TBNLC system study for the efficiency of the

pulse power system has been increased to 55% leading to a wall-plug-to-rf efficiency of 50%. As we learn more about the technology, we may introduce new design changes which could alter the cost and efficiency estimates. Yet, on the basis of the work that has been performed thus far, we can safely argue that the cost of upgrading the initial NLC configuration to one or more-TeV-c.m. energy is an attractive option.

In regard to the beam dynamics issues, we have offered conceptual solutions for longitudinal beam stability as well as BBU control for both the low-frequency component, associated with induction gaps, and the high-frequency component, associated with rf extraction cavities. These concepts are supported by detailed simulations. We hope to have demonstrated by these studies that the solutions offered have a reasonable chance of success.

We would like to stress that the reported work is an ongoing effort. Further theoretical and computation studies are being conducted. Specifically, cavity design work continues, in particular in relation to the issue of how to minimize the transverse defocusing on the beam envelope, and the induction cavity design is being optimized to achieve the needed longitudinal as well as transverse impedances. Feedback systems are being studied to relax the constraints on energy flatness and quadrupole field errors. Our experimental program allows for hardware development, verification of theory/simulations, and improvement of our cost estimates. At the scheduled completion of our experiments in 2002, the TBNLC could be seriously considered for a 1.5-TeV NLC upgrade.

References

[Allen 1989] M.A. Allen *et al.,* "High Gradient Electron Accelerator Powered by a Relativistic Klystron", *Phys. Rev. Lett.* **63**, 2472 (1989).

[Allen 1991] S.L. Allen *et al.,* "Measurements of Reduced Corkscrew Motion on the ETA-II Linear Induction Accelerator", *Proc. of the 1991 Part. Acc. Conf.*, 3094–3096 (1991).

[Barnard 1991] J. Barnard *et al.,* "Study of Recirculating Induction Accelerators as Drivers for Heavy Ion Fusion", UCRL–LR–108095 (1991).

[Brigg 1985] R.J. Brigg *et al.,* "Theoretical and Experimental Investigation of the Interaction Impedances and Q Values of the Accelerating Cells in the Advanced Test Accelerator", *Particle Acclerators* **18**, 41 (1985).

[Calame 1991] J.P. Calame and W.G.Lawson, "A Modified Method for Producing Carbon-Loaded Vacuum-Compatible Microwave Absorbers from a Porous Ceramic", *IEEE Trans. Electron. Devices* **38**–6, 1538–1543 (June 1991).

[Chen 1990] Y.-J. Chen, "Corkscrew Modes in Linear Accelerators", *Nucl. Instr. and Methods* **A292**, 455–464 (1990).

[Chen 1992] Y.-J. Chen, "Beam Control in the ETA-II Linear Induction Accelerator", *Proc. of the 1992 LINAC Conf.*, 540–544 (1992).

[Clark 1988] J. Clark *et al.*, "Design and Initial Operation of the ETA-II Induction Accelerator", *Proc. 14th Int'l Linac Conf.*, Williamsburg, VA, 19–23 (1988).

[Chattopadhyay 1990] S. Chattopadhyay, ed. "Impedance Beyond Cutoff", Special edition of *Particle Acclerators* **25**, Nos. 2–4 (1990).

[Deford 1989] J.F. Deford, G.D. Craig, and R.R. McLead, "The AMOS (Azimuthal Mode Simulator) Code", *Proc. of the 1989 Part. Acc. Conf.*, Chicago, IL (1989).

[Deford 1990a] J.F. Deford and G. Kamin, "Application of Linear Magnetic Loss of Ferrite to Induction Cavity Simulation", *Proc. 1990 Linear Accel. Conf.*, Albuquerque, NM, 384–386 (1990).

[Deford 1990b] J.F. Deford *et al.*, "The AMOS Wakefield Code", *Proc. Conf. on Computer Codes and the Linear Acc. Community*, Los Alamos, NM, 265–289 (1990).

[Fessenden 1992] T. Fessenden and C. Fong eds. "Induction Linac Systems Experiments Conceptual Design Report", LBL–PUB–5324 (1992).

[Giordano 1995] G. Giordano *et al.,* "Beam Dynamic Issues in an Extended Relativistic Klystron", *Proc. of the 1995 Part. Acc. Conf.* (1995).

[Griffith 1990] L.V. Griffith and F.J. Deadrick, "Progress in ETA-II Magnetic Field Alignment Using Stretched Wire and Low Energy Electron Beam Techniques", *Proc. of the 1990 Linac Conf.*, 423–425 (1990).

[Haimson 1965] J. Haimson, "Injector and Waveguide Design Parameters for a High Energy Electron-Positron Linear Accelerator", *IEEE Trans. Nucl. Sci.* **NS-12**–3, 499–507 (June 1965).

[Haimson 1970] J. Haimson, "High Duty Factor Electron LINACS", in *Linear Accelerators,* P.M. Lapostolle and A.L. Septier eds., 462–466. (North-Holland, Amsterdam, 1970).

[Haimson 1989] J. Haimson, and B. Mecklenburg, "Design and Construction of a Chopper Driven 11.4-GHz Traveling Wave RF Generator", *Proc. of the 1989 Part. Accel. Conf.,* 243–245 (1989).

[Haimson 1992] J. Haimson, and B. Mecklenburg, "Suppression of beam induced pulse shortening modes in high power RF generator and TW output structures", *Proc. SPIE Symposium on Intense Microwave and Particle Beams III*, Vol. **1629–71**, 209 (1992).

[Halbach priv] K. Halbach, private communication.

[Halbach 1980] K. Halbach, *Nucl. Instr. and Methods* **169**, 1–10 (1980).

[Hogan 1992] W.J. Hogan, R. Bangerter, and G.L. Kulcinski, "Energy from Inertial Fusion", *Physics Today* **42**–9, 42–50 (1992).

[Houck 1992a] T.L. Houck, and G.A. Westenskow, "Status of the Choppertron Experiments", *Proc. 16th Int'l Linac Conf.*, Ottawa, Ontario, Canada, 498–450 (1992).

[Houck 1992b] T.L. Houck, G.A. Westenskow, and S.S. Yu, "BBU Code Development for High-Power Microwave Generators", *Proc. 16th Int'l Linac Conf.*, Ottawa, Ontario, Canada, 495 (1992).

[Houck 1993] T.L. Houck, "Design Study of a Microwave Driver for a Relativistic Klystron Two-Beam Accelerator", *Proc. of the 1993 Part. Acc. Conf.*, Washington, DC, 2590 (1993).

[Kapetanakos 1985] C.A. Kapetanakos, and P. Sprangle, "Ultra-high-current electron induction accelerators", *Physics Today* **38**, 58 (1985).

[Kroll 1990] N.M. Kroll, and D.U.L. Yu, "Computer determination of the external Q and resonant frequency of waveguide loaded structures", *Particle Acclerators* **34**, 231–250 (1990).

[Lee 1978] E.P. Lee, "Resistive Hose Instability of a Beam with the Bennett Profile", *Physics of Fluids* **21**, 1327 (1978).

[Li 1994] H. Li, T.L. Houck, S.S. Yu, and N. Goffeney, "Design Consideration of Relativistic Klystron Two-Beam Accelerator for Suppression of Beam-Breakup", *Proc. SPIE Symposium on Intense Microwave Pulses II*, **2154**–10, 91–98 (1994).

[Orzechowski 1986] T.J. Orzechowski *et al.*, "High-Efficiency Extraction of Microwave Radiation from a Tapered-Wiggler Free-Electron Laser", *Phys. Rev. Lett.* **57**, 2172 (1986).

[Panofsky 1968] W.K.H. Panofsky and M. Bander, "Asymptotic Theory of Beam Break-up in Linear Accelerators", *Rev. Sci. Instr.* **39**, 206 (1968).

[Ryne 1990] R.D. Ryne, and S.S. Yu, "Relativistic Klystron simulations using RKTW2D", *Proc. of the 1990 Linear Acc. Conf.*, Albuquerque, New Mexico, 177–179 (1990).

[Sessler 1982] A.M. Sessler, "The free-electron-laser as a power source for a high gradient accelerating structure", Workshop on Laser Acceleration of Particles, NY, *AIP Conference Proceedings* **91**, 154 (1982).

[Sessler 1987] A.M. Sessler and S.S. Yu, "Relativistic-Klystron Two-Beam-Accelerator", *Phys. Rev. Lett.* **58**–23, 2439–2442 (1987).

[Siemann 1993] R.H. Siemann, "Overview of Linear Collider Designs", *Proc. of the 1993 Part. Acc. Conf.*, Washington, DC, 532–536 (1993).

[Thompson 1993] K.A. Thompson *et al.*, "Design and simulation of accelerating structures for future linear colliders", SLAC–PUB–6032 (Nov. 1993).

[Westenskow 1994] G.A. Westenskow and T.L. Houck, "Results of the Reacceleration Experiment: Experimental Study of the Relativistic-Klystron Two-Beam-Accelerator Concept", *Proc. of the 10th Int'l Conf. on High Power Particle Beams*, San Diego, CA (1994).

Contributors

- Fred Deadrick
- Guido Giordano
- Enrique Henestroza
- Tim Houck
- Hai Li
- Steve Lidia
- Louis Reginato
- David Vanecek
- Glen Westenskow
- Simon Yu